


Magnetohydrodynamic equilibrium and stability properties of the Infinity Two fusion pilot plant

J.C. Schmitt¹ , D.T. Anderson¹ , E.C. Andrew¹ , A. Bader¹ ,
K. Camacho Mata¹ , J.M. Canik¹ , L. Carbajal¹ , A. Cerfon¹ ,
W.A. Cooper^{1,2} , N.M. Davila¹ , W.D. Dorland¹ , J.M. Duff¹ ,
W. Guttenfelder¹ , C.C. Hegna¹ , D.P. Huet¹ , M. Landreman¹ , G. Le Bars¹ ,
A. Malkus¹ , N.R. Mandell¹ , B. Medasani¹ , J. Morrissey¹ , T.S. Pedersen¹ ,
P. Sinha¹ , L. Singh¹ , Y. Suzuki³ , J. Varela¹ and K. Willis¹ 

¹Type One Energy Group, Knoxville, TN 37931, USA

²Swiss Alps Fusion Energy (SAFE), Vers l'Eglise, Switzerland

³Graduate School of Advanced Science and Engineering, Hiroshima University,
Higashi-Hiroshima, Japan

Corresponding author: J.C. Schmitt, john.schmitt@typeoneenergy.com

(Received 2 December 2024; revision received 18 March 2025; accepted 18 March 2025)

The magnetohydrodynamic (MHD) equilibrium and stability properties of the Infinity Two fusion pilot plant baseline plasma physics design are presented. The configuration is a four-field period, aspect ratio $A = 10$ quasi-isodynamic stellarator optimised for excellent confinement at elevated density and high magnetic field $B = 9$ T. Magnetic surfaces exist in the plasma core in vacuum and retain good equilibrium surface integrity from vacuum to an operational $\beta = 1.6$ %, the ratio of the volume average of the plasma and magnetic pressures, corresponding to 800 MW deuterium–tritium fusion operation. Neoclassical calculations show that a self-consistent bootstrap current of the order of ~ 1 kA slightly increases the rotational transform profile by less than 0.001. The configuration has a magnetic well across its entire radius. From vacuum to the operating point, the configuration exhibits good ballooning stability characteristics, exhibits good Mercier stability across most of its minor radius and it is stable against global low- n MHD instabilities up to $\beta = 3.2$ %.

Key words: fusion plasma

1. Introduction

In the following, we assess the magnetohydrodynamic (MHD) equilibrium and stability properties of the Infinity Two fusion pilot plant (FPP) baseline plasma physics design. Infinity Two is a four-field period, aspect ratio $A = 10$, quasi-isodynamic (QI)

configuration with optimised confinement at elevated density and high magnetic field ($B = 9$ T) (Hegna *et al.* 2025). An explicit goal of the optimisation was to demand robust magnetic surface integrity by avoiding low-order rational surfaces in the confinement region. For a configuration with a number of field periods (NFPs), this implies avoiding values of $\iota = (\text{NFP}/M)$, $(2 \times \text{NFP}/M)$, $(3 \times \text{NFP}/M)$, where M is a small integer, typically of the order of $1-2 \times \text{NFP}$. Additionally, the high-field approach used in the generation of Infinity Two allows for the desired deuterium–tritium (DT) FPP operation at relatively small β , which relaxes the constraints imposed by ideal MHD stability considerations. Here, β is the ratio of the volume averages of the plasma pressure and the magnetic pressure in the plasma:

$$\beta = \frac{2\mu_0 \langle p \rangle}{\langle B^2 \rangle}, \quad (1.1)$$

where $\langle \mathcal{L} \rangle$ indicates a volume average of the quantity \mathcal{L} . A related quantity of interest is $\beta_0 \equiv 2\mu_0 p_0 / \langle B^2 \rangle$, where p_0 is the plasma pressure at the magnetic axis.

1.1. Magnetohydrodynamic equilibrium

The MHD equilibrium and stability properties of the plasma in a stellarator fusion pilot plant must be robust and predictable. The coils of a stellarator create a three-dimensional (3-D) magnetic field topology of closed, nested toroidal flux surfaces without the need of any plasma currents. This is not a trivial task, but techniques using the concept of a winding surface (Merkel 1987; Landreman 2017) and discrete space curves (Zhu *et al.* 2018) assist with the design of filamentary coils. These filamentary coils can be further optimised to maximise the volume of nested flux surfaces (Hanson & Cary 1984; Cary & Hanson 1986; Reiman *et al.* 2007; Smiet *et al.* 2025). On any of the flux surfaces, the trajectory of the magnetic field line can be traced to evaluate the rotational transform, ι , defined as (Kruskal & Kulsrud 1958)

$$\iota = \lim_{\Delta\phi \rightarrow \infty} \frac{\Delta\theta}{\Delta\phi}. \quad (1.2)$$

The poloidal (θ) and toroidal (ϕ) angle are associated with the short and long way around the torus, respectively. When surfaces with values of ι close to low-order rationals are present within the plasma, there is a possibility that a resonant $\iota \approx n/m$ island can open under certain conditions. The field lines wrap around and connect to opposite sides of the island. Fast parallel transport along the field lines provides an additional channel for the effective radial diffusion of energy and particles across the island. Experiments on W2-A (Grieger *et al.* 1971) and W7-A (Cattanei, Dorst & Elsner 1985) both demonstrated the importance of avoiding resonant values of ι in the plasma core. The maximum stored energy that could be maintained in the plasma was severely restricted when low-order rational surfaces were present. The derivative of the transform with respect to the minor radius ρ of the plasma is called the shear, $d\iota/d\rho$. Low-shear stellarators have windows of good operation when low-order rational values of ι can be avoided in the core region. Based on consideration of the Farey tree (Meiss 1992), large windows are adjacent to low-order rationals. However, the requirement of an edge resonance enables the use of island divertor solutions (Feng *et al.* 2011; Helander *et al.* 2012). The divertor design and operation relies on the details of the resonant edge island or island remnants (Renner *et al.* 2000; Grigull *et al.* 2001; Morisaki *et al.* 2005; Feng *et al.* 2011, 2021).

1.2. MHD equilibrium limits and edge topology

Plasma-induced currents can change the field topology and location of the plasma and its edge. The plasma pressure in a stellarator generates a diamagnetic current. The variations of $1/|B^2|$ on a flux surface, combined with the divergence-free condition for the current density on that surface, $\nabla \cdot \vec{J} = 0$, requires the existence of a dipole-like current density, commonly referred to as the Pfirsch–Schlüter current (Pfirsch & Schlüter 1962). This current generates a dipole magnetic field that applies a net radial force on the plasma column. The resulting radial shift of the plasma column, called the Shafranov shift (Shafranov 1963, Freidberg 2014), sets an equilibrium limit if left uncompensated (Helander *et al.* 2012; Freidberg 2014). The neoclassical bootstrap current will alter the rotational transform and location of island structures. It also serves as a source of free energy for instabilities. For an island to serve as part of a detailed divertor design, it is essential to have good predictions regarding the edge topology at vacuum conditions, the operating point and points in between. Any sensitivities to plasma profiles and configuration details must be well understood and anticipated.

1.3. MHD stability limits in stellarators

Three-dimensional fields can be beneficial for MHD stability, when applied correctly. The Compact Toroidal Hybrid (CTH) and W7-A both demonstrated that adding a small amount of vacuum transform with helical fields to net current-carrying toroidal plasmas provided a stabilising force that would suppress vertical instabilities (ArchMiller *et al.* 2014) and provide passive disruption avoidance (Team 1980; Pandya *et al.* 2015). CTH also showed that a fractional vacuum transform of only 10 % ($\epsilon_{\text{vac}} \geq 0.07$) was sufficient to operate above the Greenwald density limit typical of tokamaks (Hartwell *et al.* 2013).

Equilibrium effects such as pressure-induced changes in the plasma shape and location, and MHD stability limits can both restrict the level of β that can be achieved. Under stable conditions, the maximum achievable limit of β is set by the available heating power and the transport properties of the configuration. The exact details vary with the configuration. In most stellarators, crossing pressure-induced MHD stability boundaries tends to lead to soft-limits on the maximum sustainable β . For example, unstable modes such as interchange and resistive ballooning mode, when present, nonlinearly saturate at benign levels without triggering large-scale crashes of the plasma (Helander *et al.* 2012; Zhou *et al.* 2024). Operating in regimes with a good magnetic well tends to stabilise the modes that would otherwise be unstable. However, current-driven sawtooth-like behaviour can become increasingly unstable in low-shear stellarators operating with ϵ close to a low-order rational (Zanini *et al.* 2020, 2021).

The relatively benign impact of surpassing pressure-induced MHD stability limits has been demonstrated in several stellarator experiments. Heliotron-E, which had the $\epsilon = 1$ surface inside the plasma (along with high shear), was found to experience pressure-driven $m/n = 1/1$ resistive-interchange modes resonant at the $\epsilon = 1$ surface with unfavourable curvature. These modes were suppressed by flattening the pressure profile to achieve $\beta \sim 2\%$ (Harris *et al.* 1984; Motojima *et al.* 1985).

The Large Helical Device (LHD) explored limits on β in a variety of configurations with different stability characteristics by varying the location of the magnetic axis, R_{ax} . The standard configuration ($R_{\text{ax}} = 3.75$ m) is only Mercier unstable in the

edge, but has poor neoclassical confinement. Its β -limit was set by general confinement properties and resistive-g mode turbulence (Yamada 2011). At $R_{ax} = 3.6$ m, the plasma is unstable against interchanges in almost the entire region because of the magnetic hill. Resistive interchange modes localised near the $\iota = 1$ surface have been observed, but the profiles were not severely degraded (Fujiwara *et al.* 2001; Komori *et al.* 2006). The $n/m = 1/2$ modes in the core can affect the profiles, but when the resonance is removed from the plasma, the degradation disappears and the temperature profiles are restored (Sakakibara *et al.* 2001). For the largest inward shift of the axis ($R_{ax} = 3.5$ m), with the highest hill, local flattening of profiles is observed, but no major collapses are seen. The onset of low- n MHD modes is consistent with linear theory of ideal interchange modes (Yamada 2011). In outward shifted configurations ($R_{ax} \geq 3.9$ m), the Mercier criterion predicts stability for interchange modes in the plasma edge at high- β , but high- n ballooning modes are destabilised by bad magnetic curvature (Varela *et al.* 2011).

High- β operations in W7-AS were notably lacking in major disruptive phenomena. The applied vertical fields led to the reduction of the magnetic well in the low- β regime, while the plasma pressure deepened it. In low- and medium- β discharges, pressure-driven low-frequency low- m modes resonant with the low-order rationals in ι were observed (Weller *et al.* 2003; Geiger *et al.* 2004). Minimising Pfirsch–Schlüter and bootstrap currents was confirmed to be desirable for stability, particularly near rational values of ι (Weller *et al.* 2003). The observation of self-stabilisation at higher β was attributed to multiple effects, including: (i) an increase in the shear; (ii) a shift of the resonance rational surface radially away from location of the steep pressure gradient and (iii) a local flattening of the pressure profile by the perturbed field (Hirsch *et al.* 2008). Comparing similar plasma conditions with and without net current, W7-AS explored the effects of tearing modes and soft disruptions that limited access to higher β values in the presence of net current (Weller *et al.* 2003). Reducing or eliminating net current helped minimise the risk of current-driven instabilities such as kink and tearing modes and disruptions (Hirsch *et al.* 2008).

W7-X was designed for high- β operation (Beidler *et al.* 1990; Grieger *et al.* 1992), with a magnetic well that deepens with β and good ballooning stability characteristics. As a QI configuration (Helander 2014), it was predicted to have favourably small Pfirsch–Schlüter and bootstrap currents at its target operating point. Experiments to explore the limiting factors on the level of β that it can achieve are planned for future campaigns. To safely create a de-tuned field for tests of MHD stability limits, experiments are planned to be performed at reduced field strength (Geiger *et al.* 2023) with a third-harmonic electron cyclotron resonance heating scheme (Erckmann *et al.* 2007). W7-X normally operates with the $\iota = 1$ resonance and $m/n = 5/5$ islands at the edge of the plasma column. By adjusting the coil currents, the rotational transform profile could be adjusted to scan the radial position of the resonance and islands in the plasma column towards the magnetic axis. Edge mode activity has been seen but no major collapses of the plasma column have occurred under normal conditions (Andreeva *et al.* 2022). With significant electron cyclotron current drive (ECCD) applied near-axis, an $\iota = 1$ crossing near the plasma axis would result in sawtooth events (Zanini *et al.* 2020; Aleynikova *et al.* 2021). Without the applied ECCD, the sawteeth were absent. As the total toroidal current increases, the radii of the $\iota = 1$ crossing also increased. Eventually, a critical limit was reached and the plasma would terminate after a collapse (Zanini *et al.* 2021).

These results confirm our understanding of when MHD instabilities are likely to occur and their consequences, such that the risk of them occurring in optimised devices can be essentially eliminated. Building upon the decades of experiments and modelling, stellarator optimisation can include targets for improved equilibrium and stability characteristics. MHD stability is required for a robust stellarator fusion pilot plant, as are a satisfactory boundary (divertor) solution, sufficient space for shielding and breeding blankets, and coils that can be constructed within engineering, manufacturing and assembly constraints. Operating at higher magnetic field strengths allows stellarators to achieve the same fusion power, P_{fusion} , at lower levels of β . This opens the configuration phase-space for optimisation of other metrics, including energetic particle confinement and turbulence optimisation, in addition to minimising the required size of the device, which are critical issues for an economical fusion power plant.

1.4. Motivation and outline

This work documents the MHD equilibrium and stability properties of a fusion pilot plant with a stable, finite- β equilibrium and an acceptable edge topology for divertor operation. The assumptions in the modelling will be discussed. The configuration is in the ‘quasi-isodynamic’ family of configurations, where $|B|$ on the flux surface approaches that of a linked-mirror. The spectrum of the finite-pressure plasma supported by the coilset, shown by Hegna *et al.* (2025), will be compared with the spectrum of the target fixed-boundary configuration. The quality of the nested flux geometry and the presence of stochastic magnetic fields or magnetic islands are checked under vacuum conditions and at finite pressure, up to and beyond the $\beta = 1.6\%$ operating point.

The configuration will be characterised with respect to its stability characteristics, including the magnetic well, stability with respect to the Mercier criterion, local ballooning modes, and global current-driven and pressure-driven MHD instabilities. The self-consistent neoclassical bootstrap current will be estimated for a range of operational plasma pressures. The Shafranov shift of the plasma column will be shown, along with its effect on the location of the O-points of the edge island.

The remainder of this paper is organised as follows. Section 2 introduces 3-D MHD equilibrium models and the numerical codes that compute the equilibrium state. The calculation of the self-consistent bootstrap current is discussed here, which is another critical characteristic of the equilibrium which has impact on scenario development and divertor design. In § 3, details of the configuration at its operating design point are presented. The general characteristics of the configuration including the self-consistent bootstrap current profiles are shown. In § 4, a scan of β is presented to explore the possible variation of bootstrap current, equilibrium features and stability with increases in plasma pressure. Several aspects of MHD stability are examined including Mercier, ballooning and global modes. We summarise and conclude in § 5.

2. 3-D magnetohydrodynamic description

The 3-D MHD equilibrium solvers, VMEC (Hirshman & Whitson 1983; Hirshman, Merkel & 1986) and HINT (Suzuki *et al.* 2006; Suzuki 2017), have been extensively used to model 3-D stellarator configurations and tokamaks. The two codes have a wide range of applicability due to the relative simplicity in their

respective models and complementary assumptions regarding closed, nested flux surfaces. The codes are adapted to parallel computing architectures and continue to be developed and maintained. They are briefly introduced here, with additional details provided in [Appendices B](#) and [C](#). More complete descriptions can be found in the above references.

2.1. Nested flux surfaces

The Variational Moments Equilibrium Code (VMEC) solves the ideal 3-D MHD equilibrium under the assumption of closed, nested flux surfaces. Islands cannot be described in the nested flux surface model assumed by VMEC. The equilibrium reconstructions discussed by Hanson *et al.* (2009, 2013) and Andreeva *et al.* (2022) provide validation of the nested flux surface model with finite plasma pressure and current. The VMEC code is the core MHD solver in V3FIT (Hanson *et al.* 2009), the 3-D equilibrium reconstruction code which is applicable to a wide variety of equilibria with 3-D fields. The free-boundary MHD solution provided by V3FIT-VMEC can be used as the starting point for higher fidelity MHD equilibrium analysis and diagnostic analyses (mode predictions, for example).

2.2. Non-nested solutions

HINT is a nonlinear 3-D MHD initial-value equilibrium code that employs a two-step relaxation method based on the dynamic equations of the magnetic field and pressure projected on an Eulerian grid (fixed in space). This grid selection allows HINT to represent islands and regions with stochastic magnetic field lines. The goal of using HINT is two-fold: (i) provide a more accurate magnetic field in the region of the edge island and (ii) provide an indication of flux surface break-up in the plasma core at finite β .

2.3. Assessment of the self-consistent bootstrap current

MHD equilibrium calculations require two profiles as input, the pressure and the toroidal current (or an equivalent quantity). The plasma pressure is calculated from the profiles of the density and temperature of each of the plasma components, $p = q \sum N \cdot T$, where $q \approx 1.6 \times 10^{-19}$ is the Coulomb charge, N is the density units of $\# \text{ m}^{-3}$ and T is in units of eV . Without an explicit external source, the current profile is determined by neoclassical physics in a stellarator. Specifically, the collisional equilibrium between bouncing and passing particles in the presence of density and temperature gradients results in a non-inductive current called the bootstrap current $J_{BS} = \langle \vec{J} \cdot \vec{B} \rangle / \langle |\vec{B}| \rangle$ (Galeev & Sagdeev 1968; Bickerton, Connor & Taylor 1971; Hinton & Hazeltine 1976; Helander & Sigmar 2005). Some general statements and estimates regarding the magnitude (and direction) of the bootstrap current can be made regarding optimised stellarators. Quasi-axisymmetric (QAS) configurations are characterised by a relatively large bootstrap current which enhances, or adds to, the rotational transform profile. Compared with QAS configurations, quasi-helically symmetric (QHS) configurations have a bootstrap current that is reduced by a factor of $1/(N_{FP} - \epsilon)$ and reversed in direction, where N_{FP} is the number of field periods of the configuration (Boozer & Gardner 1990). In a perfectly QI system, the bootstrap current would vanish (Helander & Nührenberg 2009). In practice, the bootstrap current in stellarators approximating the QI property is small (Gori, Lotz & Nührenberg 1997). Small net bootstrap currents are also predicted in quasi-poloidally symmetric devices (Spong *et al.* 2005). Even a small residual current is important to calculate

as it may affect the locations of the edge island at the divertor as well as the integrity of core rational surfaces.

Accurate calculation of the bootstrap current in stellarators requires numerical solution of the drift-kinetic equation (Hinton & Hazeltine 1976). While low-collisionality asymptotic formulae for the bootstrap current are available (Shaing & Callen 1983; Nakajima *et al.* 1989; Helander, Parra & Newton 2017), they tend to be noisy (Landreman, Buller & Drevlak 2022) and inaccurate (Albert *et al.* 2024). Including the self-consistent effect of the ambipolar solution of the radial electric field, $\vec{E}_r = -\nabla\Phi^{E.S.}$, where $\Phi^{E.S.}$ is the electrostatic potential on the flux surface, is important for neoclassical transport in stellarators (Maassberg *et al.* 1993). Although convenient semianalytic formula exist for the bootstrap current in QAS and QHS configurations (Landreman *et al.* 2022), no such formula has been found for QI.

The SFINCS code (Landreman *et al.* 2014), which is used in this work, directly solves the drift-kinetic equation in general toroidal configurations. Furthermore, it includes the effects of the radial electric field which is important in the search for the ambipolar electron- and ion-root solutions consistent with thermodynamic considerations (Shaing 1984; Turkin *et al.* 2011).

3. Operating design point

The Infinity Two FPP design is a quasi-isodynamic configuration with stellarator symmetry (Dewar & Hudson 1998). The main characteristics of the target 800 MW DT fusion power operating point are summarised in table 1, including the configuration's volume-averaged magnetic field, toroidally averaged major radius, the effective minor radius, the volume average β , the on-axis β_0 and the estimated net toroidal bootstrap current. External heating is envisaged to be provided by electron cyclotron resonance heating at 8.42 T. Continuous pellet fuelling is also required (Guttenfelder *et al.* 2025). The edge transform approaches $\iota = 4/5$. By purposely avoiding $\iota = 1$, the Infinity Two stellarator avoids the issues related to having multiple low-order resonances (1/1, 2/2, 3/3, etc.) that W7-X has had to deal with to ensure symmetric loading on the divertor plates (Andreeva *et al.* 2004; Kisslinger & Andreeva 2005; Jakubowski *et al.* 2021). The only source of current considered in this modelling is the bootstrap current, and it increases the edge transform by $\Delta\iota \approx +0.001$ compared with the same finite- β equilibrium with no net toroidal current.

The profiles used in this modelling, shown in figure 1, were informed by the high-fidelity modelling detailed by Guttenfelder *et al.* (2025). The density profile is flat for $\rho \leq 0.5$ with an on-axis value of $\sim 2.46 \times 10^{20} \text{ m}^{-3}$ and an edge density of $\sim 6.15 \times 10^{19} \text{ m}^{-3}$. The on-axis temperatures of the electrons is $\sim 17.26 \text{ keV}$ and the ions are at $\sim 13.81 \text{ keV}$. The edge temperature for both ions and electrons is 100 eV. The non-zero gradient of the ion-temperature profile is not present in the refined high-fidelity profiles (see e.g. figure 9 of Guttenfelder *et al.* (2025)), and its influence on the estimates of the bootstrap current density and MHD stability near the axis is negligible. The coil set for this configuration is described by Hegna *et al.* (2025) and shown in figure 2. It reproduces the desired target magnetic field to a high degree of accuracy with 12 coils per field period (48 coils total), while simultaneously satisfying engineering constraints on minimum coil-coil and coil-plasma distances, maximum curvature of the coils, and sufficient space for other components around the plasma. A single-filament version of the coil set was used for the modelling in this work.

Quantity	Value
Volume-averaged magnetic field strength, $\langle B \rangle$	9 T
Number of field periods	4
Toroidally-averaged major radius, R_0	12.5 m
Effective minor radius, a_0	1.13–1.25 m
β	1.6 %
β_0	4.0 %
Net toroidal bootstrap current, $I_{\text{bootstrap}}$	1 kA*
$ B _{\text{max}}/ B _{\text{min}}$ on the magnetic axis	1.68

TABLE 1. Properties of the Infinity Two FPP stellarator configuration discussed in this article.

*This bootstrap current calculation uses the multi-species SFINCS evaluations.

The interpolated magnetic grid for free-boundary VMEC evaluations was defined to span from $R \approx 8.44$ – 16.59 m, $Z \approx -3.78$ – 3.78 m, and with 180 grids in the toroidal direction over one field period. The magnetic grid for HINT evaluations used the same radial and vertical limits, but all three grids were defined to have 256 steps. Prior to using the profiles based on the high-fidelity modelling (Guttenfelder *et al.* 2025), a pressure profile that was more peaked had been assumed for the fixed-boundary version of this configuration. The coilset had been designed for those peaked profiles (not shown). The mirror-like $|B|$ on the last closed flux surface in Boozer coordinates is shown in figure 3. In the left column of figure 4, the spectrum of the field strength $|B|$ in straight field line (Boozer) coordinates for the original fixed-boundary target equilibrium (solid lines) is compared with the corresponding spectrum for the free-boundary VMEC solution (dashed lines). The boundary of the free-boundary solution was adjusted to account for the presence of the edge island structures, as described in Appendix C. The rank of the modes was determined by their individual maximum-absolute value across the entire radial profile. The x -axis for this figure is the effective minor radius, $r_{\text{eff}} = a_0\sqrt{s}$. The y -axis is a $\pm\log$ scale with unequal upper and lower limits. The rank and general shape of each of the top 20 modes of the spectrum agree well between the fixed- and free- boundary solutions, in spite of the slight change in the placement of the boundary. Furthermore, the harmonics from coil ripple ($n = 12$) are not evident. The $(m, n) = (0, 12)$ component is smaller than 10^{-3} at the magnetic axis of the VMEC solution. The right column of figure 4 is similar to the left, except that the Boozer spectrum has been replaced by that of the MHD solution with pressure profiles based on figure 1. The top 20 modes are the same as those in the left column, although the rank has changed among the last four. In spite of the different pressure profiles, the spectrum is remarkably similar, suggesting that the modifications to the spectrum due to finite- β effects may be small.

A Poincaré map at the 1/2-field period location was generated with line-following based on the vacuum fields generated by the coil set using the Julia-based MagneticFieldToolkit (Faber & Bader 2024a). The result in figure 5 demonstrates that good flux surfaces exist in this configuration even without plasma, an essential fact required for a stellarator.

Two methods were used to evaluate the vacuum rotational transform profile t_{vac} generated solely by energising the coilset. The first is via line-following, where t_{vac} is

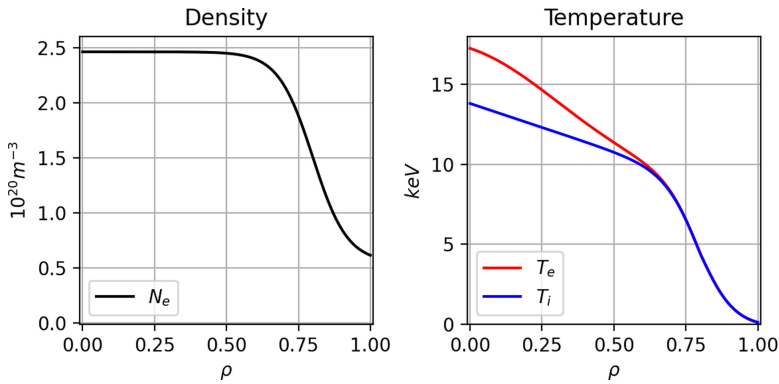


FIGURE 1. Plasma profiles informed by high-fidelity transport modelling (Guttenfelder *et al.* 2025).

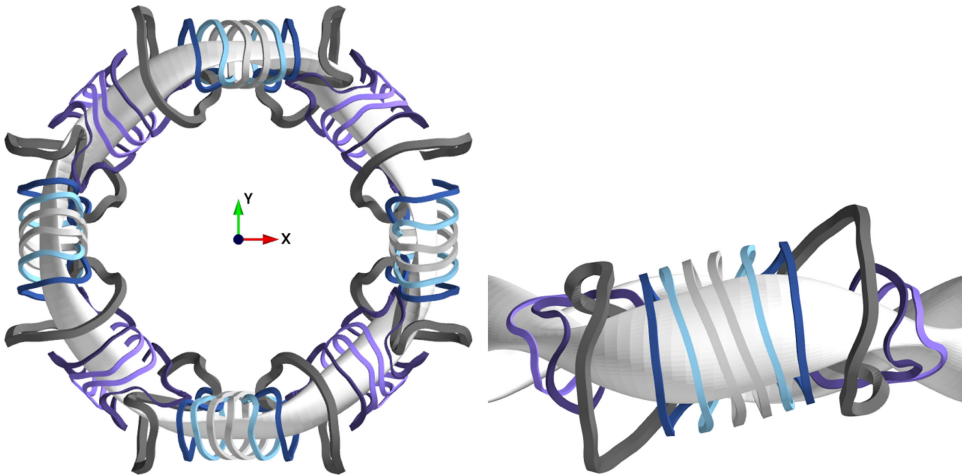


FIGURE 2. Left, top down view of a coil set with finite build for Infinity Two. There are twelve coils per field period. Right, side view of Infinity Two's coil set.

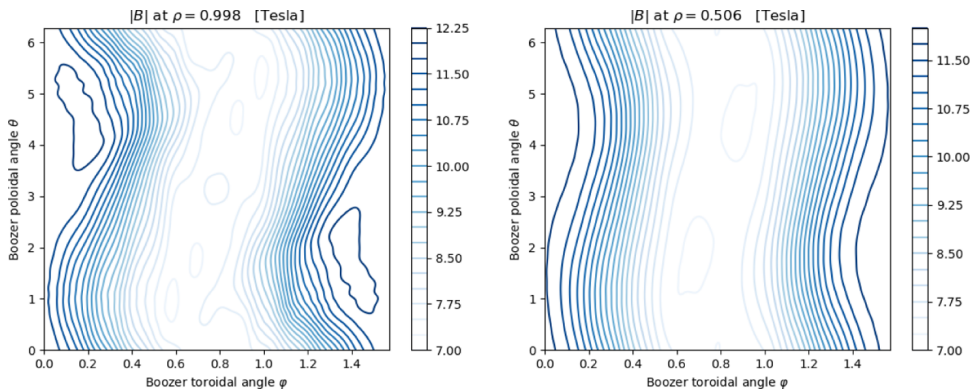


FIGURE 3. Contour plot of $|B|$ close to the last closed flux surface (left) and the mid-radius (right) of the $\beta = 1.6\%$ free-boundary VMEC MHD solution. The x - and y -axes correspond to the toroidal and poloidal angles, respectively, and span a single field period.

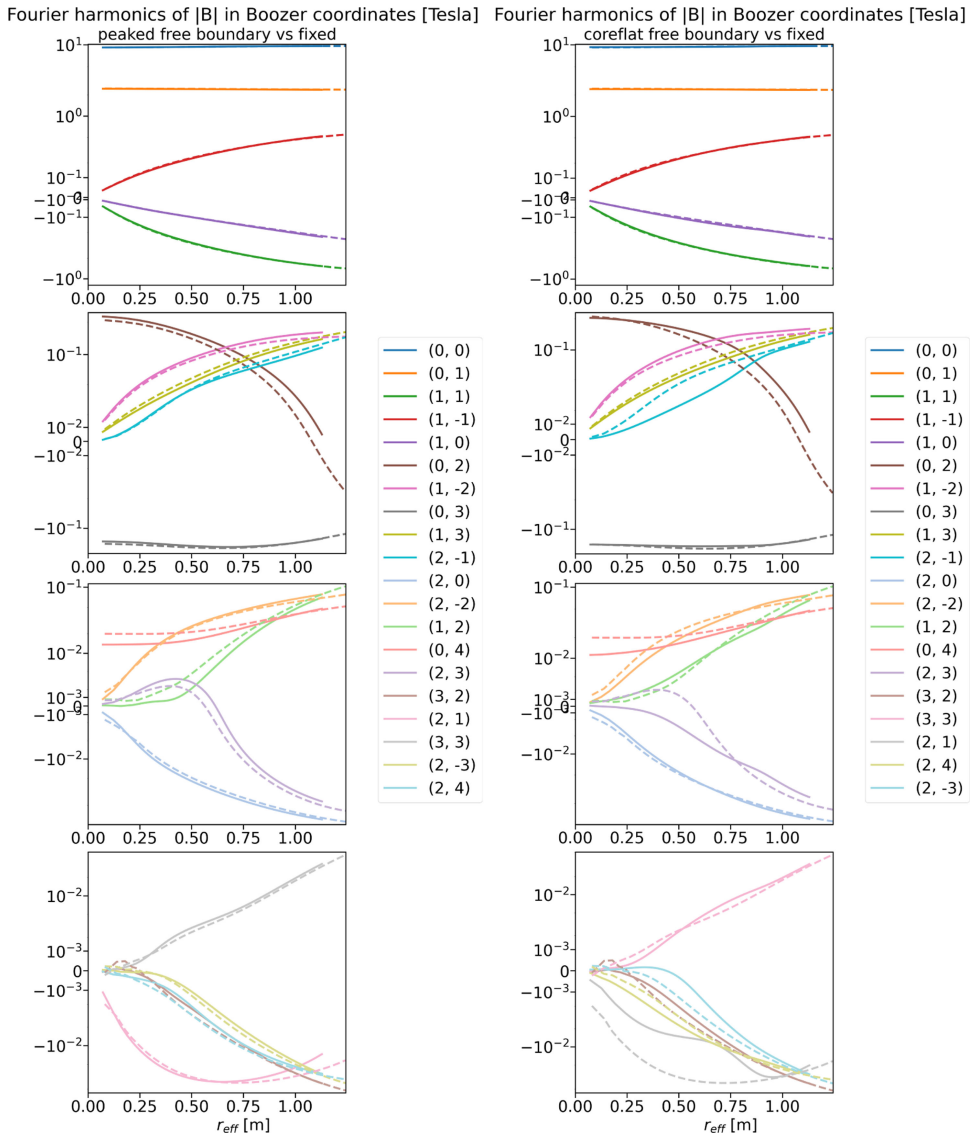


FIGURE 4. Radial profiles of the largest 20 spectral components of B in Boozer coordinates. Left column, the spectrum of the target configuration from the fixed-boundary optimisation procedure is shown as solid lines. The spectrum for the free boundary configuration is shown as dashed lines with the same colour scheme as the fixed boundary spectrum. The y-axis is a logarithmic scale (sign-preserving) and the x-axis is $\rho = \sqrt{\psi_t/\psi_{t,\text{LCFS}}}$. Numbers in the legend indicate the poloidal and toroidal mode numbers (m, n) . Right column, the spectrum of the target configuration as solid lines compared with the spectrum of the free boundary solution with the profiles from figure 1. The same 20 modes populate the top ranks, but the order of the last four is different.

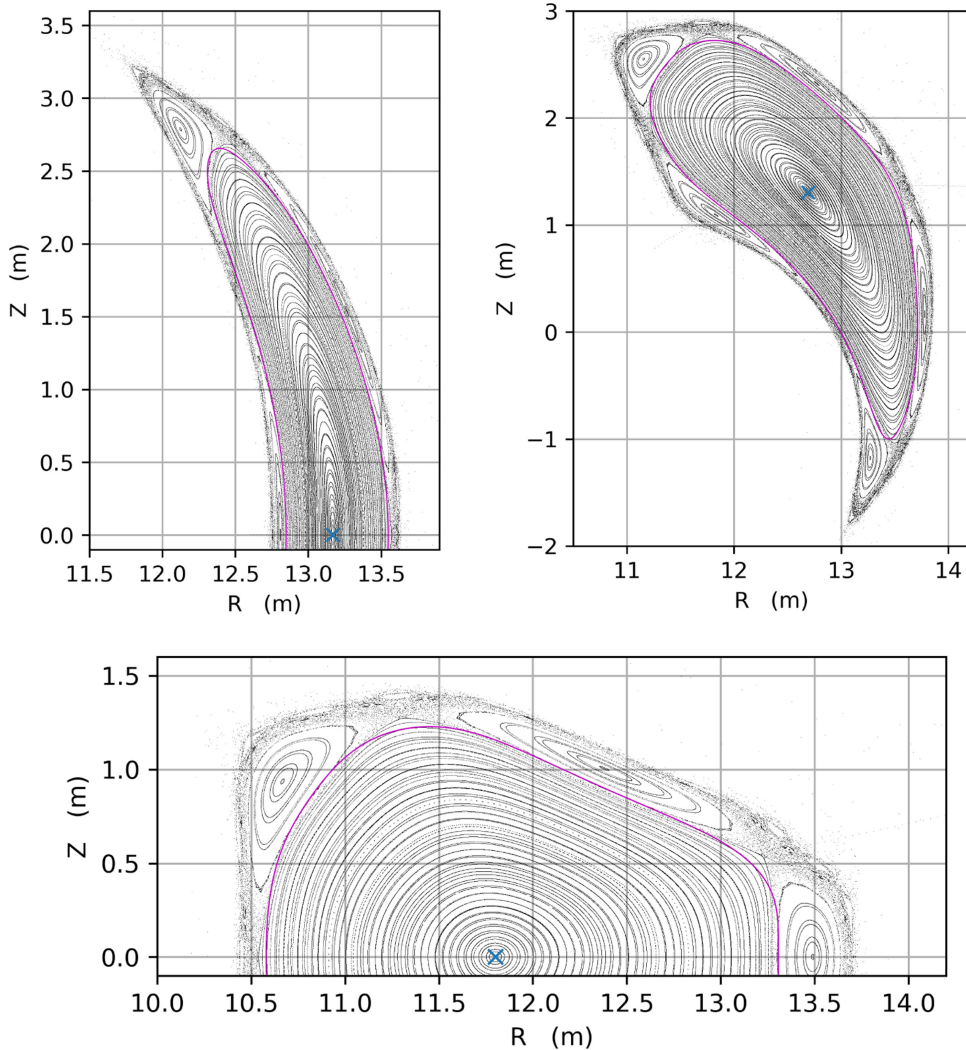


FIGURE 5. Black points, Poincaré map at $\phi = 0, \pi/8$ and $\pi/4$ for the magnetic field generated only by coils. Well-formed closed flux surfaces form the core of the confinement region and an $\iota = 4/5$ island is in the edge. Magenta line and blue \times , the LCFS and magnetic axis of the free boundary vacuum VMEC solution, respectively.

estimated by (1.2) for several field lines launched at the $Z = 0, \phi = 0$ plane with the value of R varied to scan across the minor radius. The second evaluation of ι_{vac} is from the free-boundary VMEC solution which calculates the transform as $\iota \equiv d\psi_p/d\psi_t$, the ratio of the differential change in poloidal (ψ_p) and toroidal (ψ_t) magnetic fluxes enclosed within a surface. The two methods are compared in figure 6 and agree well, with differences noted near the magnetic axis, where VMEC results converge slowly with the number of surfaces in the radial grid NS . As described in Appendix B, this vacuum solution was converged with $NS = 165$, $MPOL = NTOR = 14$ and $FTOL = 1.5e-11$. To achieve better on-axis convergence for the vacuum case, $NS = 300$ or higher may be required.

Species	Relative concentration
D	0.425
T	0.425
He	0.05
W	1.5×10^{-5}
Ne	0.004892

TABLE 2. Relative concentrations of deuterium, tritium, helium, tungsten and neon for multi-species self-consistent bootstrap current evaluations.

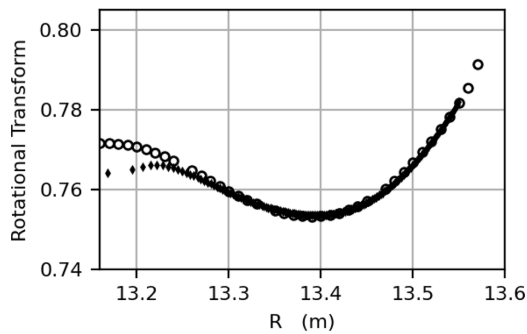


FIGURE 6. Comparison of rotational transform profiles for the vacuum configuration. The circles correspond to t_{vac} computed via field line tracing and the diamonds correspond to t_{vac} computed from the VMEC free-boundary equilibrium.

Self-consistent estimates of the bootstrap current for the profiles shown in [figure 1](#) were established for the free-boundary configuration. The left panel of [figure 7](#) shows the profiles of the neoclassical bootstrap current for a two-species electron–hydrogen plasma with $T_H = T_i$, $N_H = N_e$ from [figure 1](#). A multi-species scenario which more closely models that of a burning fusion reactor is also considered. The relative ratios of the plasma species are listed in [table 2](#), and all ion species are assumed to be in thermal equilibrium (for all ions ‘X’, $T_X = T_i$ from [figure 1](#)). The ambipolar radial electric field solution for both of these scenarios is shown in the right panel of [figure 7](#). In the two-species case, the ion-root is the only stable solution found at all radii, except for the points nearest the magnetic axis ($\rho \leq 0.10$) where the electron-root was found to also be stable. In this specific case, the evaluation of (D.2) predicts that the ion-root is the most likely solution. Even so, the effect on the bootstrap current would likely be minimal as the differences in parallel current are small at $\rho = 0.05$ and negligible at $\rho = 0.10$ ([figure 7](#), left). In the multi-species case, only one root is stable at all radii and the solution near the core is positive for $\rho \leq 0.1$, which may help expel high-Z impurities near the axis. The total bootstrap current at the target operating point is estimated to be small. In the two-species case, $I_{\text{bootstrap}} \approx 2$ kA and in the multi-species case, $I_{\text{bootstrap}} \approx 1$ kA. The effect of the total bootstrap current at $\beta = 1.6\%$ is to add to the rotational transform.

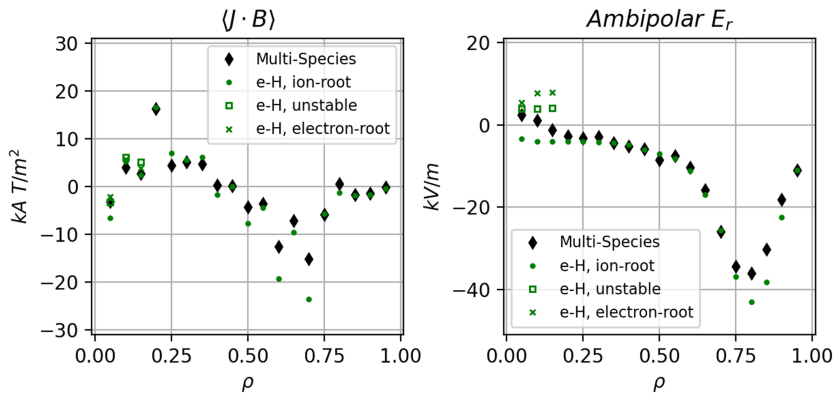


FIGURE 7. Left panel, the neoclassical bootstrap current $\langle J \cdot B \rangle$ for two-species electron-hydrogen plasmas (green markers) and multi-species plasmas (black diamonds) with profiles of figure 1 and relative ratios listed in table 2 for the multi-species case. Right panel, ambipolar radial electric field solution for cases shown in the left panel. The stable solution is the ion-root for the two species (e–H) case.

The adiabatic invariant is a measure of the quasi-isodynamic quality of the configuration, defined by

$$J = \int m v_{\parallel} dl. \quad (3.1)$$

In the ideal limit, $J = J(\psi)$, the J contours correspond to surfaces of constant radius. In figure 8, the contours of adiabatic invariant, (3.1), are shown for different choices of the pitch angle variable λ_n for the fixed-boundary $\beta = 1.6\%$ equilibrium (top row), the free-boundary $\beta = 1.6\%$ equilibrium (middle row) and the free-boundary vacuum solution (bottom row). Here, $\lambda_n^2 = B_{\max}(1 - \mu B_{\min}/\mathcal{E})/(B_{\max} - B_{\min})$ denotes a particle with energy \mathcal{E} and magnetic moment μ moving along a field line with minimum (maximum) value of magnetic field strength given by B_{\min} (B_{\max}). Here, $\lambda_n \rightarrow 0$ denotes deeply trapped particles and $\lambda_n \rightarrow 1$ denotes barely trapped particles. In these plots in polar coordinates, the flux surface label ρ and the field line angle label α are mapped to the radial and angle coordinates, respectively.

Evaluations with HINT at the $\beta = 1.6\%$ operating point were performed. The pressure profiles in the HINT simulation were parabolic in ρ , and the peak value was adjusted to match $\beta = 1.6\%$ of the operating point. Poincaré maps generated with the HINT solution are shown in figure 9 as black dots. The enclosed toroidal flux of the VMEC solution was adjusted so that the LCFS of each simulation matched to within approximately 0.4 Wb. The LCFS of the free-boundary VMEC solution is shown in magenta, which lies close to the LCFS of the HINT solution just inside the O-points of the resonant $(m, n) = (5, 4)$ island that defines the boundary of this configuration. The magnetic axis of the VMEC solution, shown as a blue 'X' is well aligned with the axis of the HINT solution. In the same figure, the blue circles represent selected surfaces of the vacuum solution (magnetic axis, O-points of the island and two surfaces close to the plasma/island interface).

The edge $\iota = 4/5$ island is robustly present, and has moved only slightly from its vacuum position, a combination of both a small-yet-finite pressure-driven Shafranov

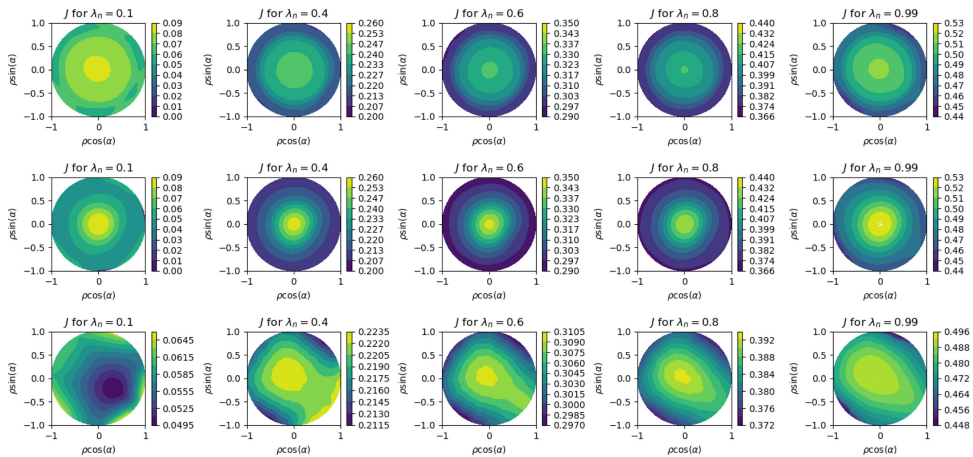


FIGURE 8. Polar plots (ρ versus θ) of the second adiabatic invariant, J_{inv} for a range of bounce parameter, λ . Top row, fixed-boundary $\beta = 1.6\%$ configuration; middle row, free-boundary solution at $\beta = 1.6\%$; bottom row, free-boundary vacuum solution. Good poloidal closure of the J_{inv} contours is seen in both the fixed- and free- boundary finite beta solutions. Minor differences can be seen between the two finite beta solutions. The quality of the poloidal closure is degraded somewhat in the vacuum solution.

shift (which can also be seen as a shift in the magnetic axis from its vacuum location) and a very small change in the rotational transform, which modifies the location of the ϵ -resonance location in the radial direction. The connection length of the field lines, the rotational transform and fractal dimension were monitored for indications of the formation of islands and stochastic regions. In the core portion of the plasma column, no regions of chaos or internal islands larger than 0.5 cm have formed and pressure contours overlap with the Poincaré maps (not shown).

4. Feasibility of the operating point

To assess the feasibility of reaching the $\beta = 1.6\%$ operating point, along with the equilibrium and stability properties around the design point, a series of test scenarios were developed as a proxy for low- to high- β operation. While not a true pilot-plant scenario development exercise, it provides insight into the robustness, stability and feasibility expected of the operating design point. The test scenarios assume the same temperature profiles as the target operating point. The shapes of the density profiles are retained, but the magnitude of the density profiles was scaled down/up. This effectively scales the operating plasma pressure, β and β_0 by the same factor. For each scenario, the enclosed toroidal flux was adjusted to match the boundary of a corresponding HINT simulation with the same effective β , as discussed in [Appendix C](#). Next, the self-consistent bootstrap current profile was calculated with free-boundary VMEC solutions while the net toroidal flux was held constant. For simplicity, a two-species electron–hydrogen plasma was assumed in this scan. The radial profiles of the plasma pressure, bootstrap current density and rotational transform are shown in [figure 10](#). [Table 3](#) shows the variation of the net current, the change in $\epsilon(s = 1)$ due to the bootstrap current, $\Delta\epsilon_{LCFS}$, and the average radial location of the magnetic axis.

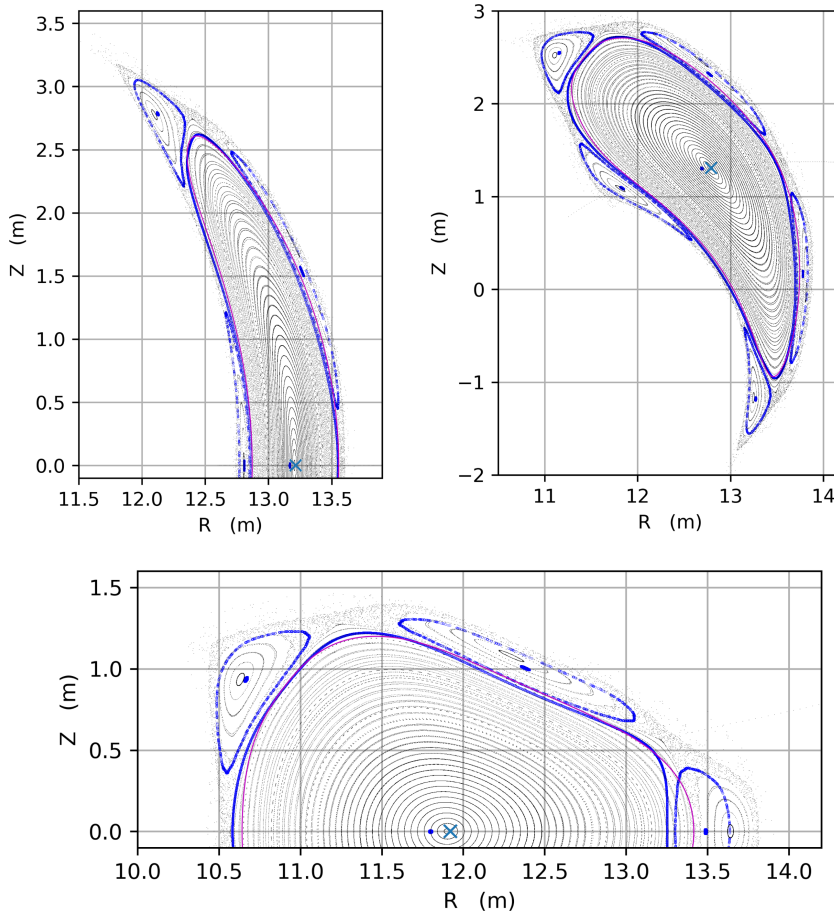


FIGURE 9. Poincaré maps from HINT simulation for $\phi = 0, \pi/8$ and $\pi/4$ at the $\beta = 1.6\%$ operating point shown as black points. The axis of the plasma column and island at vacuum and two surfaces close to the plasma/island interface in vacuum are shown in blue. The blue 'X' is the magnetic axis of the finite $\beta = 1.6\%$ VMEC evaluation. The last closed flux surface of the VMEC solution at the target operating point is shown as a magenta line.

The Shafranov shift is linear with β , as expected, and the value of $\iota(s=1)$ of the MHD solution is only slightly influenced by the net bootstrap current. It may be necessary to demonstrate control of the island O-point location and size, either through re-optimisation of the configuration, compensation with the actuation of a set of external control coils or combination of the two. The classical divertor design proposed by Bader *et al.* (2025) is anticipated to function with no need of extra control, but the local island backside divertor would likely require fine control to operate as intended. It is anticipated that it will be sufficient to control the island position and shape with actively controlled external island-control coils similar to the control and/or planar coils of W7-X (Risse *et al.* 2018). The net current peaks when the density is scaled to approximately half its nominal value. From this peak, it reduces until it is nearly completely eliminated at a test scenario with the density scaled by 125%. At higher values of β , the bootstrap current reverses direction and increases in magnitude.

β	β_0	$\psi_T(\rho = 1)$ Wb	$ I_{bootstrap} $ (kA)	$\Delta t_{LCFS, I_{Bootstrap}}$	$\langle R_{axis} \rangle$ (m)
Vacuum	0	34.8	—	—	12.45
0.8	1.9	33.6	8	+ 0.002	12.47
1.6	4.0	33.4	2	+ 0.001	12.49
2.0	5.0	34.4	≤ 1	~ 0	12.50
2.4	6.1	33.6	3	−0.001	12.51
2.9	7.2	33.6	9	−0.002	12.52
3.3	8.3	33.6	14	−0.002	12.53
3.7	9.5	33.6	18	−0.005	12.54
4.2	10.7	33.4	27	−0.007	12.56

TABLE 3. Global equilibrium properties as a function of increasing plasma density for an electron–hydrogen plasma. β , β_0 , total bootstrap current, its effect on the edge transform and the toroidally averaged radius of the magnetic axis.

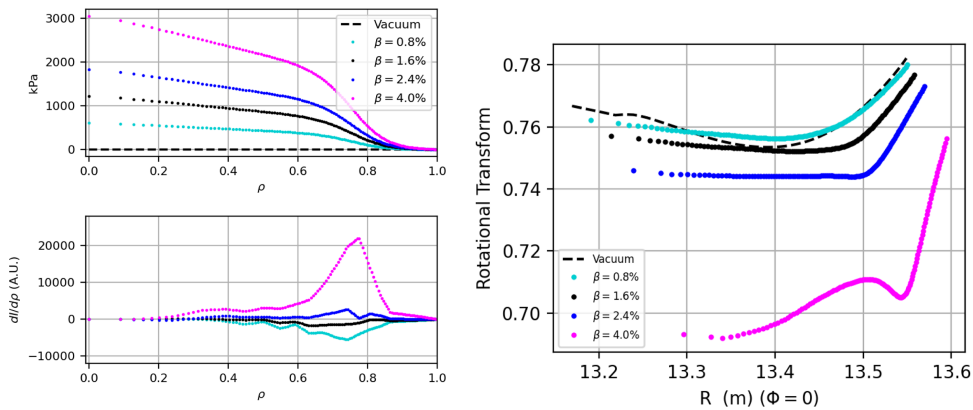


FIGURE 10. Left (top), plasma pressure profile for several test cases examined here. Left (bottom), toroidal current density profile for the same cases. Here, an electron–hydrogen plasma was assumed. Right, rotational transform profiles for the density scan.

4.1. Low-density test scenarios, bootstrap current and ambipolar radial electric field

The ambipolar E_r -solution is predicted to be entirely in the ion-root at the target operating point. In the test scenarios with an operating density below the target operating point, the ambipolar E_r -solutions have a stable electron-root near the magnetic axis, and in some cases, the ion-root disappears entirely at the inner-most radii leaving only an electron-root solution, as shown in figure 12. The radial location of the transition from ion-root to electron-root is chosen to minimise the generalised heat production, where multiple solutions exist. However, the diffusion equation establishing the width of this transition region has not been solved in this specific low-density case, but will likely be necessary as part of more complete scenario development exercises for plant operation where a wider variety of profiles would be explored.

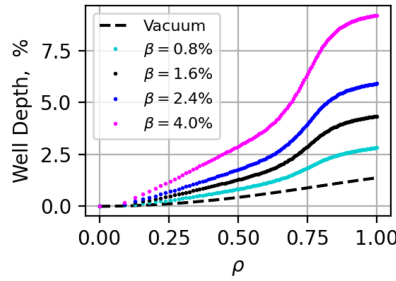


FIGURE 11. Magnetic well depth for test cases shown in figure 10. The magnetic well increases from $\sim 1.5\%$ in vacuum to above 8% at $\beta = 4.0\%$.

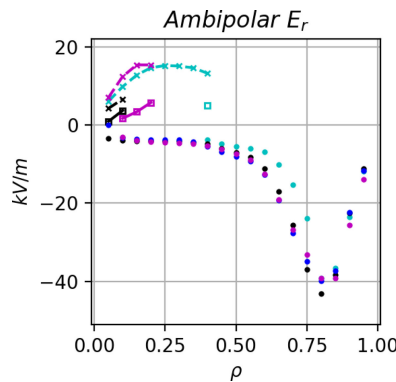


FIGURE 12. Ambipolar radial electric field solution E_r for the cases shown in figure 10. $\beta = 0.8\%$ (dark turquoise) is in the electron-root $\rho < 0.3$ and in the ion-root otherwise. The target operating point, $\beta = 1.6\%$ (black) has only a small region near the axis that has multiple stable roots. At $\beta = 2.4\%$ (blue), the electron-root solution vanishes entirely. At $\beta = 4.0\%$, (magenta) the electron-root reappears as the only stable solution near the axis, $\rho \leq 0.1$.

4.2. High-density test scenarios, bootstrap current, equilibrium limits and stability predictions

In the scenarios with β above the target operating point, the net bootstrap current reduces to zero and then reverses direction shown in figure 13. The effect on the rotational transform profile is to reduce its value. While the $n/m = 3/4$ is not a value that resonates with the equilibrium's field periodicity (although $n/m = 12/16 = 0.75$ does), it could potentially play a role in stellarator symmetry breaking magnetic island formation, the stability of global MHD modes (discussed in § 4.3.3) and Alfvén eigenmodes (Carbajal *et al.* 2025). Of course, in practice, the rational surface can be avoided by adding rotational transform through auxiliary coils if required. Fine control of the rotational transform has been demonstrated in W7-X (Andreeva *et al.* 2004).

HINT simulations for the scenarios at the elevated $\beta = 4\%$ predict that a higher-order $m = 11$ island appears near the periphery of the plasma, radially closer to the magnetic axis than the $\iota = 0.80$ edge island resonance (see figure 14). Furthermore, the Shafranov shift of the magnetic axis differs by approximately 2 cm.

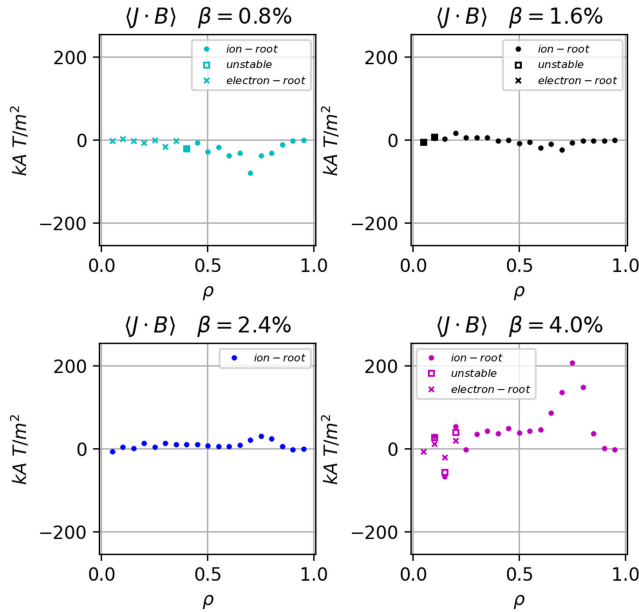


FIGURE 13. Radial profile of the bootstrap current $\langle J \cdot B \rangle$ for electron–proton plasmas for cases shown in figure 10. The net bootstrap current changes sign from low β to high β , with almost no net current at $\beta = 2.0\%$ (not shown). The difference in localised current densities between the electron- and ion-roots is small in these cases.

At elevated levels of plasma pressure, the simulation predicts that the nested flux surfaces will break and an internal island will develop. However, other soft limits set by stability considerations may play a role before the plasmas were to reach a level of $\beta \sim 4\%$, as discussed in the next section. Nonetheless, these simulations indicate that the Infinity Two FPP configuration has robust magnetic surface integrity up to β values well beyond that required for 800 MW DT fusion operation.

4.3. Stability predictions

4.3.1. Mercier stability

The Mercier criterion can be expressed as (Bauer, Betancourt & Garabedian 1984; Carreras *et al.* 1988)

$$D_{\text{Mercier}} = D_S + D_W + D_I + D_G \geq 0. \quad (4.1)$$

As shown in figure 15, Mercier stability is satisfied across the majority of the radial profiles, and the stability characteristics improve with increasing plasma pressure. The individual terms of (B.3) are plotted in figure 16. The shear of the transform is small in the core and steep near the edge. The profile of D_S shows that regions close to zero shear have a destabilising influence, and the radial location and span vary with β . The edge is always stabilising. The profile of the magnetic well term (D_W) shows a stabilising effect that improves with β . The D_I -term, related to the net toroidal current, is destabilising at low β . With increasing pressure, the net bootstrap current decreases and the D_I -contribution becomes stabilising for part of the outer half of the plasma core, $0.5 < \rho < 0.8$ at $\beta \sim 1.6\%$. It continues to become more stabilising with increasing pressure, even when the bootstrap current changes

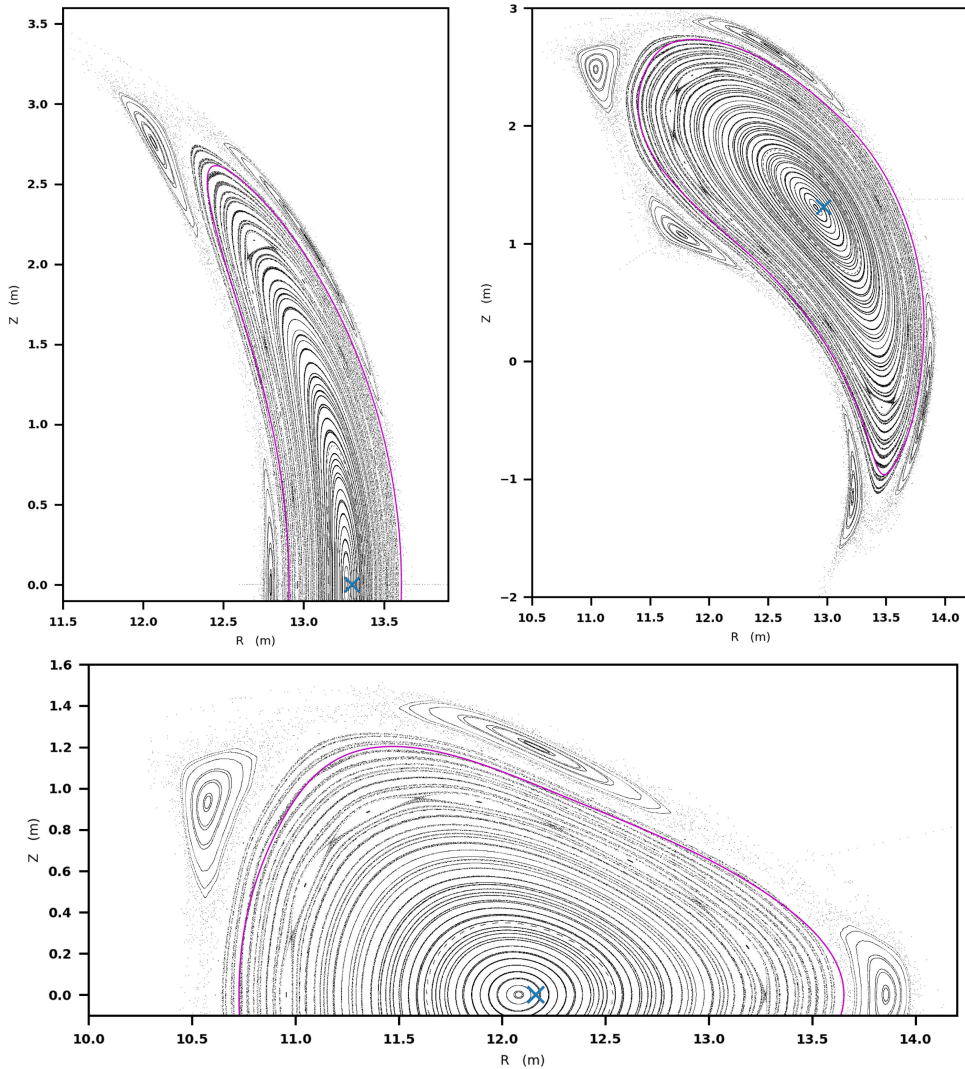


FIGURE 14. HINT results with elevated pressure at $2.5\times$ higher than the base operating point, with $\beta \sim 4\%$. One island forms in the periphery, with $m = 11$, and the edge becomes more stochastic compared with the operating point, [figure 9](#).

direction and increases in magnitude, except for the region near $\rho \sim 0.7$, where the current density is the largest. The D_G term is destabilising, and its effect grows with β . Across most of the radius, the largest terms are D_W and D_G by 2–3 orders of magnitude. The terms are closer in magnitude near the edge, with D_G being the largest at low- β . The net stabilising effects of the terms related to the increased well depth, shear and current more than compensate for the destabilising effect of the geodesic curvature term, as seen in [figure 16](#).

4.3.2. Infinite- N ballooning stability

Ballooning modes are localised along a field line in regions of unfavourable curvature (Freidberg [2014](#)). The modes are destabilised when the pressure gradient,

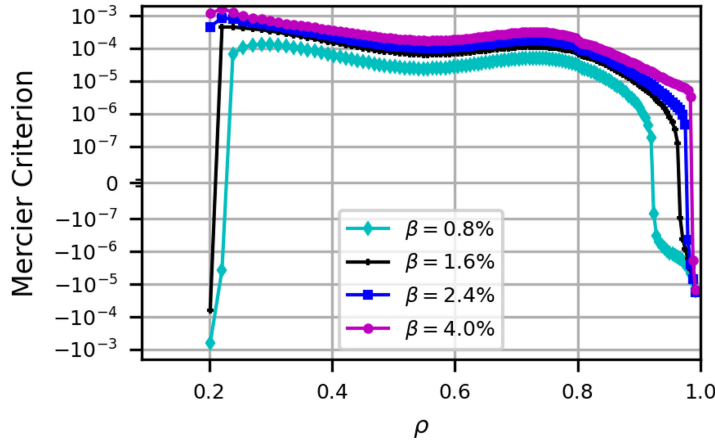


FIGURE 15. Radial profile of the Mercier criterion from $\beta = 0.4\%$ to $\beta = 4.0\%$. The radial extent of the Mercier stable region increases with β , primarily due to the deepening magnetic well (see figure 16).

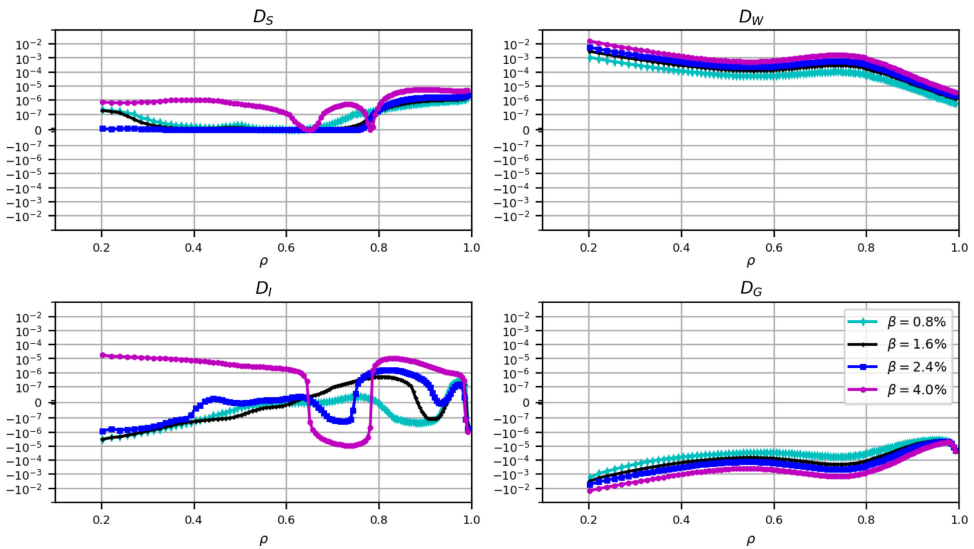


FIGURE 16. Radial profiles of the components of the Mercier criterion from $\beta = 0.4\%$ to $\beta = 4.0\%$. The largest terms are related to the magnetic well (D_W , which is stabilising and improves with β , see figure 11) and the geodesic curvature (D_G , which is destabilising and worsens with β). Where the shear of the transform is close to 0, the stabilising shear term, (D_S) is also close to 0. The shear is always stabilising for $\rho > 0.8$. The current term (D_I) tends to destabilise at the lowest β , but at higher β , it becomes a stabilising term, except for certain radially localised regions, e.g. close to $\rho \sim 0.7$ where the bootstrap current density is largest at $\beta = 4\%$.

$p' = (dp)/(ds)$, is above some threshold. Stabilisation occurs through magnetic field-line bending (Hegna & Nakajima 1998).

For each of the equilibria described above, ballooning stability was evaluated with the COBRAVMEC code (Sanchez, Hirshman & Ware 2000) and the Julia-based

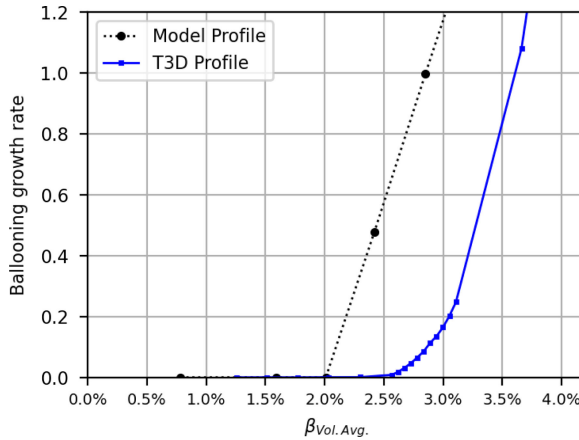


FIGURE 17. Peak growth rate for ballooning modes versus the plasma β for three different profile shapes. Model profile, the profiles from figure 1 result in a conservative limit, $\beta \sim 2\%$; T3D profile, scans with self-consistent profiles predict a higher limit, $\beta = 2.5\%$. The modified profiles result in reduced transport at the locations of strong ballooning drive.

adaptation available in *StellaratorOptimizationMetrics* (Faber & Bader 2024b). For the profiles in figure 1, the configuration is stable against ballooning modes up to $\beta \approx 2\%$. The standard ballooning analysis considers only up to $k_w = 10$ helical wells, which predicts stability in the region for $\rho > 0.9$ even though the Mercier criterion is strictly violated. If the analysis is extended to account for very long wavelengths, $k_w = 300$, the ballooning growth rate is positive, consistent with Mercier. Above that, regions that are ballooning unstable develop near $\rho \approx 0.7\text{--}0.8$. This unstable region grows in radial extent and the growth rates increase with β . In practice, however, this should not be viewed as a β -limit of the configuration. At high operating β , kinetic ballooning modes emerge in the turbulent transport simulations which have the effect of lowering the gradients in the vicinity of the ideal ballooning stability boundary. The profiles of figure 1 were informed by the high-fidelity modelling of Guttenfelder *et al.* (2025). Further analysis in that same work develops a converged, self-consistent transport solution with profiles which have reduced pressure gradients in the edge region. If those profiles, shown in figure 9 of Guttenfelder *et al.* (2025), are used for the β scan instead of the model profiles of figure 1, the ideal ballooning onset occurs near $\beta = 2.5\%$. Indeed, the self-consistent transport modelling has the effect of shifting the location of the trouble spots to a slightly larger radial location, $\rho \approx 0.75\text{--}0.85$.

4.3.3. Finite- N global MHD stability

The ideal MHD stability of magnetically confined plasmas is described by a variational formulation of the linearised equations of motion coupled with the continuity equation, an equation of state that governs the pressure evolution, Maxwell's equations that includes Ampère's law, and Ohm's law. This was formulated by Bernstein *et al.* (1958) and serves as the basis for the development of computer codes to investigate tokamaks, reversed field pinches, stellarators and other confinement systems. For stellarator configurations, the assumption has relied on MHD equilibrium states with nested magnetic flux surfaces, until quite recently. Recent work

(Kumar *et al.* 2022) has demonstrated that a multi-region relaxed variational principle can be used to predict linear and ideal MHD stabilities using the stepped pressure equilibrium code (Hudson *et al.* 2012). Here, however, we use the nested flux surface model.

The Infinity Two FPP configuration considered here is stable to global ideal MHD modes at low and intermediate toroidal mode numbers n at $\beta = 1.6\%$. Figure 18 shows that the configuration becomes unstable to low $n < 15$ modes only when β exceeds 3.5 %. From the possible set of toroidal resonances, the most unstable low- n mode we have computed at $\beta = 3.7\%$ corresponds to that of the $n = 1$ mode family ($n = \pm 1, \pm 3, \dots \pm 11, \dots$) in which the $m/n = 16/11$ component is dominant (a brief description of the resolution and mode families is in Appendix F).

We display on the right of figure 18 the profiles of the leading Fourier amplitudes corresponding to the perturbed radial magnetic field $\delta \vec{B} \cdot \nabla s \equiv \delta B^s$ for the $N = 1$ family. The particular normalisation chosen in this plot ($\sqrt{g} \delta B^s / \psi'_i(s)$) is in dimensionless units to facilitate cross-configuration and cross-device comparisons. The radial magnetic field structure impact on phenomena such as fast ion transport would constitute a critical issue at the elevated β , but at the target operating point, the problem does not exist. The bottom row displays the eigenvalues for the three distinct mode families as a function of β for low toroidal mode numbers $n < 15$. The left plot uses a linear scale and the right plot uses a semi-log scale for the y -axis. Stable modes at the continuum are always near the marginal point $\lambda = 0$. Hence, the logarithm of $\ln(|\lambda|)$ will be very negative. Only the significantly unstable modes will be large in this plot. The dashed line indicates the value of $\lambda = -0.001$. So any value of $\ln(|\lambda|)$ less than this corresponds either to a stable mode or a weakly unstable mode. Very localised unstable mode structures near the core of the plasma can become destabilised. We consider these modes spurious as a result of the poor reconstruction of the derivative of the equilibrium pressure in the vicinity of the magnetic axis.

5. Summary and discussion

The Infinity Two FPP configuration presented in this work includes a candidate coil set and a set of plasma profiles that are expected to reach fusion conditions. The operating density was scaled as a proxy to study low- to high- β operating scenarios. Poincaré maps constructed with line-following of the vacuum fields show that good flux surfaces are present. HINT evaluations at the operating point, along with subsequent post-processing line-following, demonstrate that good flux surfaces are also predicted from vacuum up to the finite β operating point. The edge topology changes only slightly within the target operating range. The configuration is robust against ballooning modes, is stable against low- n and high- n global MHD modes, and has a stabilising magnetic well, which deepens with β , across the entire profile from vacuum up to its operating point. This indicates that a clear path from vacuum to the operating point exists in terms of controlling the edge island structure for divertor operations. It is expected to achieve stationary finite- β conditions without disruptive activity and with minimal need to control external coil currents for island position control.

At elevated levels of β above the target operating point, the depth of the magnetic well continues to increase. Ballooning modes with the profiles presented here are stable up to $\beta = 2.0\%$. Above that, regions of bad curvature near the $\rho \approx 0.7$ – 0.8 radius appear to go unstable first. However, that prediction is a conservative one.

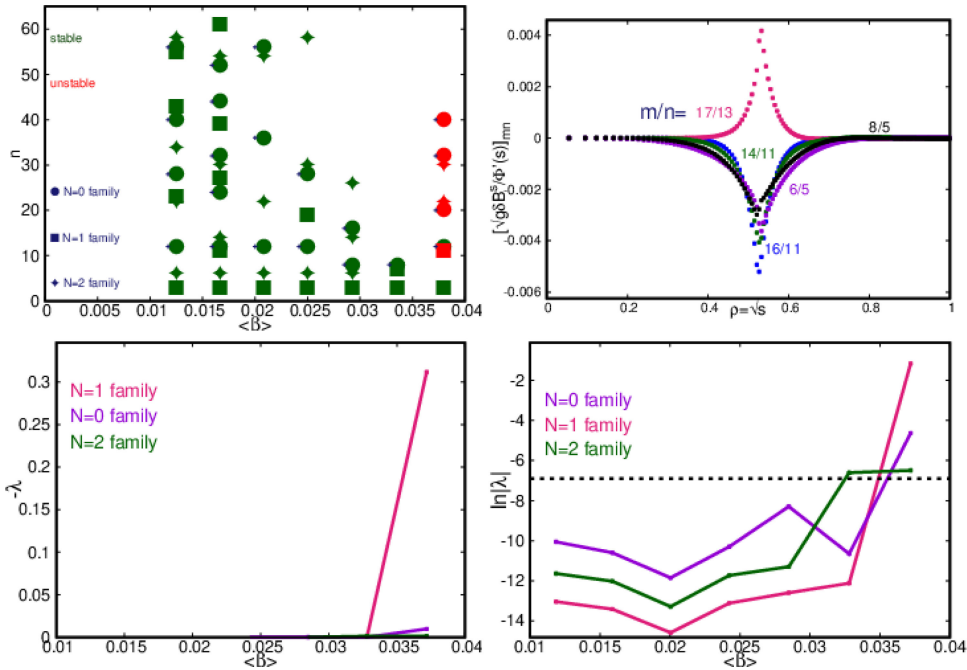


FIGURE 18. Global stability. Top left, the circles indicate modes of the stellarator symmetry breaking $n = 0$ family, squares represent periodicity breaking modes of the $n = 1$ family and diamonds correspond to modes of the $n = 2$ family (they impose two-fold periodicity around the torus). The symbols in green identify stable modes and the red symbols represent more global unstable modes that appear at high $\beta > 3.5\%$. Top right, radial profiles of the five leading amplitudes of $\sqrt{g\delta B^s}/\Phi'(s)$ at $\beta = 3.7\%$ for the unstable mode where the $m/n = 16/11$ component is dominant. The bottom row displays the eigenvalues for the three distinct mode families as a function of β for low toroidal mode numbers $n < 15$. Left, linear scale. Right, semi-log scale.

The self-consistent transport modelling (Guttenfelder *et al.* 2025) predicted a reduction of the transport to alleviate the strong ballooning drive near $\rho \sim 0.7$. Evaluations with the self-consistent profiles predicted an ideal ballooning limit of $\beta = 2.5\%$ with the location of the most unstable ballooning modes at the outer radii of $0.75 \leq \rho \leq 0.85$. Global MHD modes exhibit regions of very localised instability near the core at pressures just above the $\beta = 1.6\%$ operating point, but these are considered spurious. Global low- n modes are stable up to $\beta = 3.2\%$. Large global instabilities of the $N = 1$ family are expected to appear at the highest values of pressure explored in this work.

Several important items are left for future work. Manufacturing, assembly and placement errors of the field coils can result in magnetic field errors that can degrade the quality of flux surfaces, change the magnetic spectrum, alter stability limits, affect the neoclassical bootstrap current and negatively affect transport properties. Anticipating and including the uncertainties related to the coil set as-built will rely on the MHD models as part of the analysis workflow. Performing full-torus evaluations with HINT will be critical to confirm that no symmetry-breaking errors are present. Nonlinear simulations with stellarator geometries will also provide confidence of the stability of the operating point (Schlutt *et al.* 2013; Sovinec *et al.* 2022;

Ramasamy *et al.* 2024; Wright & Ferraro 2024). The sensitivity of the operating point to uncertainties in the profiles will be explored in the future. While the Shafranov shift is projected to be proportional to β , the bootstrap current can be quite sensitive to changes in the profiles. However, like other QI configurations, this device exhibits the feature of having low to no bootstrap and small Pfirsch–Schlüter currents, and is predicted to experience small distortions and motions of the plasma column as the plasma pressure increases. Plasma flows are neglected or artificially damped in the both VMEC or HINT. The quasi-isodynamic configuration does not have a preferred direction of symmetry and plasma flows, if present, are expected to be small. Large internal islands are not present and the HINT simulations predicts robust flux surfaces up to the operating point. Regardless, if islands were to develop, such as in the simulated $\beta = 4.0\%$ case, even small residual plasma flows may be sufficient to ‘heal’ them (Narushima *et al.* 2008; Hegna 2011). No extra control is required for the classical divertor design proposed by Bader *et al.* (2025), but the local island backside divertor would likely require actively controlled external island-control coils similar to the control and/or planar coils of W7-X (Risse *et al.* 2018) for fine control of the island position and shape.

Acknowledgements

We gratefully acknowledge the use of the computational resources managed and supported by Princeton Research Computing, a consortium of groups including the Princeton Institute for Computational Science and Engineering (PICSciE) and the Office of Information Technology’s High Performance Computing Center and Visualization Laboratory at Princeton University.

Editor Per Helander thanks the referees for their advice in evaluating this article.

Funding

We gratefully acknowledge the use of National Energy Research Scientific Computing Center (NERSC) resources, a Department of Energy Office of Science User Facility using NERSC award FES-ERCAP27470.

Declaration of interests

The work of M.L. and W.D. was performed as consultants and was not part of the employees’ responsibilities to the University of Maryland. The work of J.V. was performed as a consultant and was not part of the employee’s responsibilities at the University of Texas.

Appendix A. Magnetic well

In a toroidal geometry, the specific volume, U , is a flux-surface quantity defined as the change in volume with respect to increasing enclosed toroidal flux ψ_t (Miyamoto 1987):

$$U = dV/d\psi_t \equiv \int \frac{dl}{|B|}. \quad (\text{A.1})$$

The integral is evaluated along a magnetic field line on the flux surface and $|B|$ is the magnitude of the magnetic field along the field line. When the derivative of the specific volume is positive, $dU/d\psi_t > 0$, a destabilising magnetic hill is present. A negative derivative, $dU/d\psi_t < 0$, indicates a magnetic well. The depth of the magnetic well as a function of radius is defined by (Wakatani 1998)

$$-\frac{\Delta U}{U} = \frac{U_{\text{axis}} - U(\rho)}{U_{\text{axis}}}. \quad (\text{A.2})$$

A positive gradient of the well depth indicates a region with a magnetic well and a negative gradient indicates a region with a magnetic hill.

Appendix B. VMEC

The Variational Moments Equilibrium Code (VMEC) solves the ideal 3-D MHD equilibrium under the assumption of closed, nested flux surfaces. The model assumes a static isotropic plasma with no fluid flows is sought that satisfies:

$$\vec{F} = \vec{J} \times \vec{B} - \nabla p = 0, \quad (\text{B.1a})$$

$$\vec{J} = \frac{1}{\mu_0} \nabla \times \vec{B}, \quad (\text{B.1b})$$

$$\nabla \cdot \vec{B} = 0, \quad (\text{B.1c})$$

$$p = p(s), \quad (\text{B.1d})$$

where \vec{J} is the plasma current density, \vec{B} is the total magnetic field, p is the plasma pressure and μ_0 is the permeability of free space. An inverse coordinate representation is employed: $\vec{X} = \vec{X}(s, \theta, \zeta)$, where s is the flux surface label, and θ and ζ are poloidal and toroidal angles, respectively. The default radial grid is uniform in $s = \psi_t / \psi_{t, \text{LCFS}}$, where ψ_t is the enclosed toroidal flux and LCFS stands for last closed flux surface. The coordinates R and Z of the surfaces are expanded in two-dimensional (2-D) Fourier series in poloidal angle θ and toroidal angle ζ . In VMEC, ζ is equal to the laboratory toroidal angle ϕ . Islands cannot be described in the nested flux surface model assumed by VMEC. The boundary can either be a fixed constraint or an initial guess. In the first case, the boundary geometry is taken as an input to the computation, and the boundary condition $\vec{B} \cdot \vec{n} = 0$ is imposed there: the computational boundary acts as a perfectly conducting wall and surface currents flowing in that perfectly conducting wall contribute to holding the plasma in force balance inside the boundary. This describes the fixed-boundary VMEC calculations. In contrast, in free-boundary VMEC calculations, the plasma is held in force balance by external coils, and the location of the plasma boundary is computed self-consistently together with the plasma equilibrium. Specifically, the equilibrium is considered to be achieved when the residual force, \vec{F} , in (B.1a), is satisfied everywhere inside the plasma, and when the jump of the sum of the plasma pressure and the magnetic pressure across the plasma boundary is zero (to within some numerical accuracy) (Hirshman *et al.* 1986).

For the VMEC evaluations listed in table 3, the number of poloidal modes (MPOL), the maximum toroidal mode number (NTOR), the number of radial surfaces and the desired residual force-balance of the VMEC solution are shown in table 4. Using fewer than 12 poloidal harmonics leads to inaccurate estimates of the rotational transform near the magnetic axis, and using more than 14 harmonics prohibits reliable VMEC convergence. The number of surfaces in the computations grid (NS) can be increased at the cost of minimal achievable FTOL and increased computational runtime.

Parameter	Vacuum	Finite- β
MPOL	14	12
NTOR	14	12
NS	165	124
FTOL	1.5×10^{-11}	1×10^{-16}

TABLE 4. Fourier spectrum, radial grid and residual force balance parameters for the VMEC vacuum and finite- β evaluations in this work.

B.1 Mercier

The Mercier criterion (Mercier 1962) can be expressed as (Bauer *et al.* 1984; Carreras *et al.* 1988)

$$D_{\text{Mercier}} = D_S + D_W + D_I + D_G \geq 0. \quad (\text{B.2})$$

The individual terms are the stabilising (> 0) or destabilising (< 0) contributions of the shear (D_S), magnetic well (D_W), current (D_I), and geodesic curvature (D_G). These are expressed as

$$D_S = \frac{s}{t^2 \pi^2} \frac{(\psi'_t \psi'_p)^2}{4}, \quad (\text{B.3a})$$

$$D_W = \frac{s}{t^2 \pi^2} \int \int \sqrt{g} d\theta d\zeta \frac{B^2}{g^{ss}} \frac{dp}{ds} \left(V'' - \frac{dp}{ds} \int \int \sqrt{g} \frac{d\theta d\zeta}{B^2} \right), \quad (\text{B.3b})$$

$$D_I = \frac{s}{t^2 \pi^2} \left[\int \int \sqrt{g} d\theta d\zeta \frac{B^2}{g^{ss}} \psi''_t I' - (\psi''_t \psi'_p) \int \int \sqrt{g} d\theta d\zeta \frac{\vec{J} \cdot \vec{B}}{g^{ss}} \right], \quad (\text{B.3c})$$

$$D_G = \frac{s}{t^2 \pi^2} \left[\left(\int \int \sqrt{g} d\theta d\zeta \frac{\vec{J} \cdot \vec{B}}{g^{ss}} \right)^2 - \left(\int \int \sqrt{g} d\theta d\zeta \frac{(\vec{J} \cdot \vec{B})^2}{g^{ss} B^2} \right) \left(\int \int \sqrt{g} d\theta d\zeta \frac{B^2}{g^{ss}} \right) \right]. \quad (\text{B.3d})$$

Here, the Jacobian is $\sqrt{g} = 1/\nabla s \cdot \nabla \theta \times \nabla \zeta$, g^{ss} is the metric element $g^{ss} = |\nabla s|^2$ and $V'' = dV/ds$. The domain of integration is over the entire flux surface, $\theta \in [0, 2\pi]$, $\zeta \in [0, 2\pi]$. The terms of the Mercier criterion are evaluated by VMEC in the post-processing stage.

Appendix C. HINT

HINT is a nonlinear 3-D MHD initial-value equilibrium code that employs a two-step relaxation method based on the dynamic equations of the magnetic field and pressure projected on an Eulerian grid (fixed in space). This grid selection allows HINT to represent islands and regions with stochastic magnetic field lines. The goal of using HINT is two-fold: (i) to provide a more accurate magnetic field in the region of the edge islands and (ii) to provide an indication of flux surface break-up in the plasma core at finite β .

The HINT simulation is an iterative two-step process. The first step is a relaxation of the plasma pressure profile to satisfy the condition $\vec{B} \cdot \nabla p = 0$. While \vec{B}

is held fixed, the plasma pressure at each grid point is updated for iteration $i + 1$ according to

$$p^{i+1} = \bar{p} = \frac{\int_{-L_{\max}}^{L_{\max}} \mathcal{F} p^i \frac{dl}{B}}{\int_{-L_{\max}}^{L_{\max}} \frac{dl}{B}}, \quad (\text{C.1a})$$

$$\mathcal{F} = \begin{cases} 1 & \text{for } L_C \geq L_{\max}, \\ 0 & \text{for } L_C < L_{\max}, \end{cases} \quad (\text{C.1b})$$

where L_{\max} , prescribed by the user, is the maximum length along a magnetic field line followed from each grid point in each toroidal direction (set to 10 m here); L_C is the connection length for each magnetic field line starting at each grid point. For open (closed) field lines, L_C is finite (infinite). If the connection length is shorter than L_{\max} , the averaged plasma pressure for that grid point is set to 0.

The second step is a relaxation process of the magnetic field due to plasma currents, \vec{B}_1 , for fixed p . The artificial dissipative equations are

$$\frac{\partial \vec{v}}{\partial t} = -\nabla p + \vec{J}_1 \times \vec{B} + \nu_0 \nabla^2 \vec{v} - \vec{v} \cdot (\nabla \vec{v}), \quad (\text{C.2a})$$

$$\frac{\partial \vec{B}_1}{\partial t} = \nabla \times (\vec{v} \times \vec{B} - \eta(\vec{J} - \vec{J}_{\text{net}})) + \kappa_{\text{div}B} \nabla(\nabla \cdot \vec{B}_1), \quad (\text{C.2b})$$

$$\vec{J}_1 = \nabla \times \vec{B}_1, \quad (\text{C.2c})$$

where \vec{B} is the total magnetic field due to coil currents and plasma current. The fluid velocity is given by \vec{v} . Here, η is an electrical resistivity parameter; ν_0 is the viscosity. To help accelerate convergence, these two terms are set artificially high and the mass density is normalised to 1. The $\kappa_{\text{div}B}$ -term provides numerical stabilisation to remove contributions arising from $\nabla \cdot \vec{B}_1 \neq 0$ on the computational grid. Additionally, \vec{J}_{net} is the net toroidal current defined as

$$\vec{J}_{\text{net}} = \vec{B} \frac{\langle \vec{J} \cdot \vec{B} \rangle}{B^2}. \quad (\text{C.3})$$

In the expression above, $\langle \mathcal{L} \rangle$ indicates a flux-surface average of the quantity \mathcal{L} . HINT uses the constant pressure surfaces as a proxy for the flux surfaces. The volume average of $(\nabla p - \vec{J} \times \vec{B})^2$, and the quantities $|\delta \vec{v} / \delta t|^2$ and $|\delta \vec{B} / \delta t|^2$ are monitored as measures of convergence. A typical history of these quantities is shown in [figure 19](#). The spikes in the early stages ($t < 5$) correspond to the pressure profile being applied in increasing steps, and the later spikes at $t = 20, 40, 60$ correspond to the points in the simulation when HINT resets the pressure profile distribution on the computational grid. The connection length of the field lines, the rotational transform and fractal dimension were monitored for indications of the formation of islands and stochastic regions.

C.1 Parameter settings

The HINT simulations in this work were performed on a computational mesh that spans a single field period. The number of grid points were $256 \times 256 \times 256$ in the radial \times vertical \times toroidal direction, respectively. The results of the simulations do not change significantly if the resolution is reduced to $128 \times 128 \times 128$,

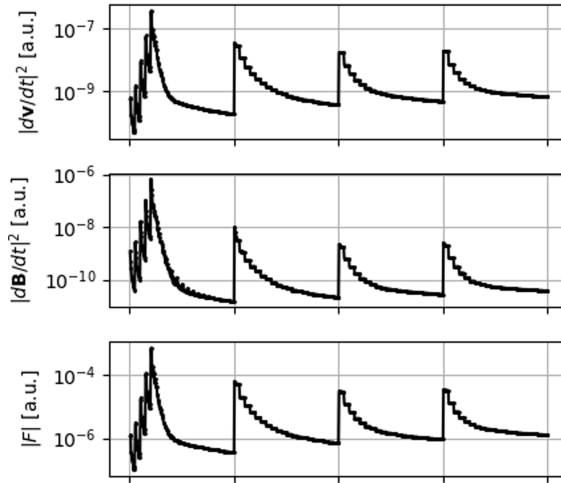


FIGURE 19. Time history of the convergence properties of the HINT simulation.

although some fidelity in the post-processed Poincaré maps is lost in the region around the edge island chain. A mesh size of $64 \times 64 \times 64$ was unreliable for HINT simulations. The simulations were evaluated for a total of 80 iterations of steps ‘A’ and ‘B’. Full-torus simulations are planned for the future to explore for the effects of symmetry-breaking errors.

C.2 Identifying the last closed flux surface of the finite- β solution

The last closed flux surface of each of the finite-beta solutions was estimated by inspecting the Poincaré maps generated with the magnetic field of the HINT simulations. The HINT simulations included the first wall model presented by Bader *et al.* (2025), but did not include either of the divertor models presented there. Detailed transport and modelling beyond the scope of this work is required to develop a self-consistent model for the edge region. To minimise the sensitivity of the edge topology to the details of the edge pressure profile gradient, pressure profiles were chosen to be linear in toroidal flux, $p(s) \propto (1 - s)$, (approximately parabolic in minor radius). The constraint on the enclosed toroidal flux of the corresponding VMEC MHD solution, PHIEDGE, was adjusted until the boundary of the VMEC evaluation aligned with the boundary of the HINT simulation, as estimated by the location of the inboard ($\theta = \pi$) and outboard ($\theta = 0$) extrema at the toroidal symmetry planes, $\Phi = 0$ and $\Phi = \pi/4$. This provides a conservative estimate of the location of the last closed surface as it does not rely on the formation of a pressure gradient in the region occupied by islands. A comparison of the normalised parabolic pressure profile at $\phi = \pi/4$, $Z = 0$, along R is shown in figure 20, top left panel. The location of the magnetic axis from the HINT and VMEC solutions are compared in the bottom left panel. For simulations up to $\beta = 3.2\%$, qualitative agreement between the VMEC and HINT boundaries and magnetic axes is observed for the parabolic profiles. In the top right panel, the pressure profile of the VMEC solution with the profiles based on figure 1 is compared with the parabolic HINT pressure profiles. The VMEC solution has the same β , but the actual peak value, β_0 , of the VMEC profile is approximately 20 % higher than the parabolic profile. At $\beta = 3.6\%$ and above, the HINT simulations begin to develop a region with a higher order

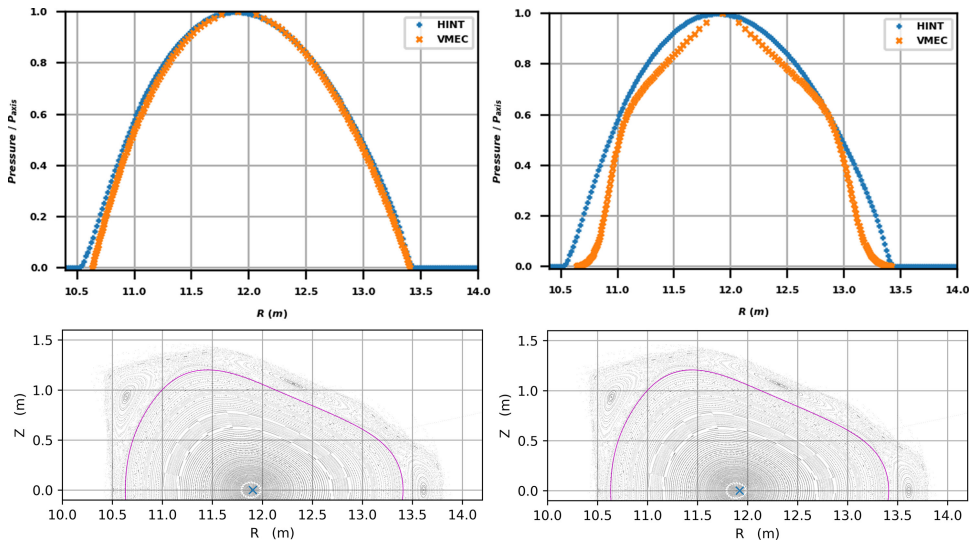


FIGURE 20. Top left, normalised pressure parabolic pressure profiles of the matched HINT and VMEC solutions. Top right, normalised parabolic pressure profile of the HINT simulation compared with the profile based on the profiles in [figure 1](#). The value of β_0 is approximately 20 % higher in the VMEC solution. Bottom row, Poincaré map based on the HINT solution (black points) and the magnetic axis (blue \times) and LCFS (magenta line) of the respective VMEC solutions from the top row.

$m = 11$ island internal to the main plasma core. The boundary region near the LCFS becomes more stochastic, reducing the overall volume of nested surfaces. The effect of the Shafranov shift is also reduced in the HINT simulations for these latter cases, compared with the VMEC solutions. An estimate of the fractal dimension (see e.g. Section 4 of Baillod *et al.* (2023)) of field lines launched at the half-field period location, $\phi = \pi/4$, $Z = 0$, $R = 10\text{--}15$ m is shown in [figure 21](#) for HINT simulations with three different levels of β . In the figure, values close to 1 indicate closed surfaces. Values close to 0 or -0.01 indicate that the field line has connected to the first wall. Values above 1 correspond to the stochastic regions near edge $m = 5$ island chain, which shifts to larger radial values at higher β . The small spikes between ~ 0.1 and ~ 0.8 are isolated high-order ($m \gg 1$) island structures. The $m = 11$ island chain develops in the $\beta = 4\%$ case, and their fractal dimension of ~ 0.6 can be seen in the figure near $R \approx 10.95$ m. No other large degradation of the closed flux surface structure is observed for the range of pressures studied in this work.

Appendix D. SFINCS

The SFINCS code (Landreman *et al.* 2014), which is used in this work, directly solves the drift-kinetic equation in general toroidal configurations. Furthermore, it includes the effects of the radial electric field which is important in the search for the ambipolar electron- and ion-root solutions consistent with thermodynamic considerations (Shaing 1984; Turkin *et al.* 2011). A single evaluation of SFINCS requires a definition of the plasma species profiles (temperatures and densities for each), the geometry of the configuration of interest, and details about the specific radial location and radial electric field value to use for the evaluation. The output of a single evaluation includes the radial fluxes of particles and heat, and the parallel flows.

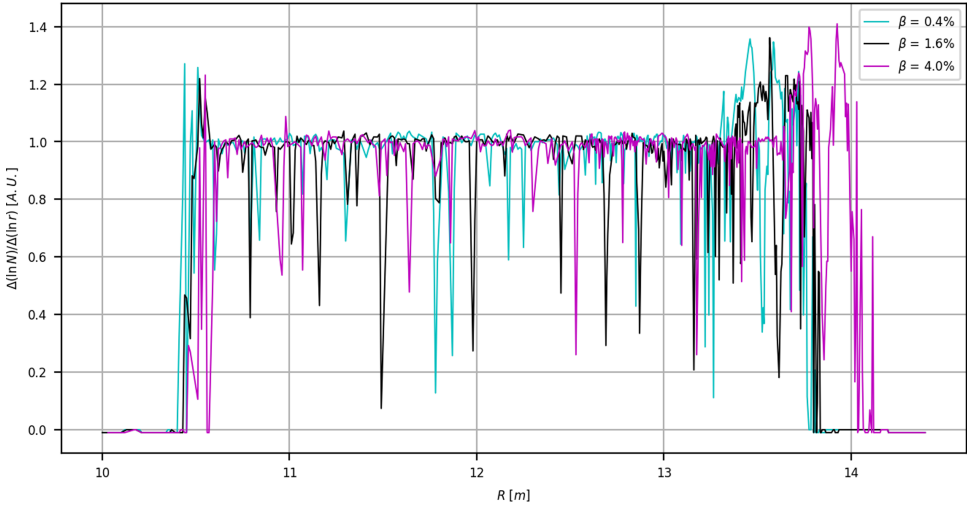


FIGURE 21. Fractal dimension for three values of β based on HINT simulations with parabolic pressure profiles.

Here, several evaluations of SFINCS are performed at each radial location with a range of values of E_r to bracket the ambipolar solution, where the radial current density, $\langle \vec{J} \cdot \nabla \rho \rangle$, equivalent to the charge-weighted sum of the radial particle fluxes Γ over each plasma species x , is 0:

$$\langle \vec{J} \cdot \nabla \rho \rangle = \sum q_x \langle \Gamma_x \cdot \nabla \rho \rangle = 0, \quad (\text{D.1})$$

where q_x is the charge of species x and $\rho = \sqrt{s}$, the square-root of the normalised toroidal flux. The bootstrap current is the charge-weighted sum of the parallel flows at the ambipolar field solution. It is possible for multiple stable ambipolar solutions to exist. Often referred to as ion-root (E_r^i) or electron-root (E_r^e), the parallel flows can be strongly modified or reduced in one regime or the other (and the influence on radial impurity transport is an important consideration). The root selected in the device is predicted by considering the minimisation of the generalised heat production (Shaing 1984; Turkin *et al.* 2011). At each radial location exhibiting multiple stable roots, the following integral is evaluated:

$$\int_{E_r^i}^{E_r^e} dE_r (Z_i \Gamma_i - \Gamma_e), \quad (\text{D.2})$$

where Z_i is the ion charge relative to the proton charge. The balance between the sum of the radial ion (i) and electron (e) currents determines which root is predicted. If the integral is positive, the ion-root is selected. The electron-root is preferred if the integral is negative.

A bootstrap current profile that is self-consistent with the plasma profiles can be established by a two-step process. In the first step, the VMEC input pressure profile is set to be consistent with the desired plasma temperature and density profiles, $p(s) = q \sum N(s) \cdot T(s)$. The initial toroidal current profile is set to 0 or provided with some initial guess. VMEC is then allowed to converge. In the second step, SFINCS evaluations provide a new estimate of bootstrap current profile using the

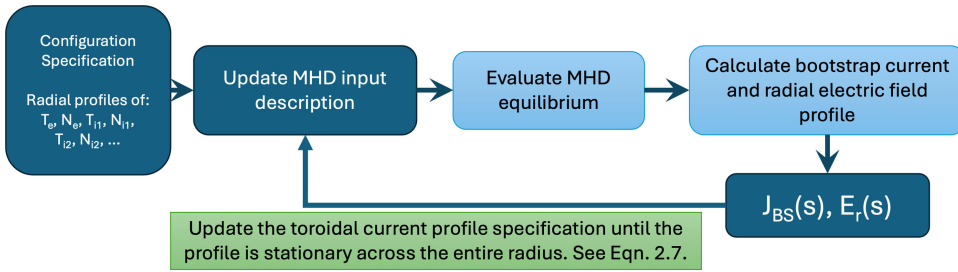


FIGURE 22. Workflow for calculating the self-consistent bootstrap current. Each iteration involves one MHD evaluation, and many evaluations of neoclassical fluxes and flows for the bootstrap current estimate. The loop continues until the toroidal current profile has converged to within some tolerance.

specified plasma density and temperature profiles along with the magnetic field and geometry information of the VMEC MHD solution. The toroidal current profile parameters in VMEC are then updated with this new estimate from SFINCS. By repeating the VMEC solution with improved estimates of the toroidal current profile provided by the SFINCS evaluations, a self-consistent estimate can be found after a few iterations. Specifically, the MHD solution and bootstrap current estimates are iterated (Watanabe *et al.* 1992) until the toroidal current density, $J_t(s)$, is self-consistent, which is defined as the condition that the toroidal current enclosed within a flux surface, $I(s) = \int_0^s ds J_t(s)$, in VMEC is consistent with the average parallel current $\langle \vec{J} \cdot \vec{B} \rangle$ calculated with SFINCS. Here, s is the normalised toroidal flux. In equilibrium, these quantities satisfy

$$\frac{dI(s)}{ds} + \frac{\mu_0 I(s)}{\langle B^2 \rangle} \frac{dp(s)}{ds} = 2\pi \frac{d\psi}{ds} \frac{\langle \vec{J} \cdot \vec{B} \rangle}{\langle B^2 \rangle} \quad (\text{D.3})$$

(see Appendix C of Landreman & Catto (2012)). When the L_1 -norm of the change to the toroidal current profile between iterations divided by the L_1 -norm of the toroidal current profile is less than some tolerance (of the order of $\sim 1\%$ in our work), or after some limit on the number of iterations is reached, the toroidal current profile is considered to be self-consistent. The number of iterations required by VMEC and SFINCS to attain a self-consistent estimate of the bootstrap current varies depending on the starting equilibrium and grid parameters of the five-dimensional (5-D) phase space of the drift-kinetic equation expansion. The workflow of this process is shown in figure 22.

D.1 Parameter settings

The parameters listed in table 5 provide well-converged solutions for SFINCS evaluations for operating points listed in table 3. Convergence tests were performed for each of the parameters for low-, medium- and high-density cases.

Appendix E. COBRAVMEC

Ballooning modes are localised along a field line in regions of unfavourable curvature (Freidberg 2014). The modes are destabilised when the pressure gradient,

Parameter	Description	Value
NXI	Number of Legendre polynomials in the pitch-angle dependence	141
NZETA	Number of grid points in toroidal angle	89
NTHETA	Number of grid points in poloidal angle	89
NX	Number of grid points in energy	7
Solver tolerance	Tolerance used to define convergence of the Krylov solver	1×10^{-7}

TABLE 5. SFINCS numerical resolutions parameters.

$p' = (dp)/(ds)$, is above some threshold. Stabilisation occurs through magnetic field-line bending (Hegna & Nakajima 1998).

Ballooning stability is computed by solving the 1-D eigenvalue equation (Correa-Restrepo 1978; Sanchez *et al.* 2001)

$$\left[\frac{d}{d\phi} \left[P(\phi) \frac{d}{d\phi} \right] + Q_1(\phi) + \lambda R(\phi) \right] F(\phi) = 0, \quad (\text{E.1})$$

where

$$P = B^\phi |k_\perp|^2 / B^2, \quad (\text{E.2a})$$

$$R = \frac{P}{(B^\phi)^2}, \quad (\text{E.2b})$$

$$Q_1 = \frac{\epsilon^2 \beta_0 p' \kappa_s}{B^\phi} \quad (\text{E.2c})$$

and the inverse aspect ratio is $\epsilon = a/R_0$, where a and R_0 are the minor and major radii. Here, B^ϕ is the toroidal contravariant component of \vec{B} , k_\perp is the perpendicular wavevector and κ_s is the normal curvature.

For the ballooning stability evaluations shown in figure 17, field lines on the flux surface were chosen to be centred on a 2-D mesh in the poloidal and toroidal directions. The field lines locations were separated by 18° in the poloidal direction, starting at $\theta = 0$. The lines were separated by 6° in the toroidal direction starting at the $\Phi = 0$ location. Several radial surfaces were analysed, ranging from $s = 0.05$ to $s = 0.95$ in increments of 0.05. The estimated number of helical wells included in the analysis permitted in the evaluation was selected from 1, 3 and 10, with 10 always providing the most restrictive limit of the stability.

Appendix F. TERPSICHORE

The ideal MHD stability of magnetically confined plasmas is described by a variational formulation of the linearised equations of motion coupled with the continuity equation, an equation of state that governs the pressure evolution, Maxwell's equations that includes Ampère's law, and Ohm's law. This was formulated by Bernstein *et al.* (1958) and serves as the basis for the development of computer codes to investigate tokamaks, reversed field pinches, stellarators and other confinement systems. For the stellarator configurations analysed here, we will assume an MHD equilibrium state with nested magnetic flux surfaces.

Here, the stability of a plasma is determined from the evaluation of the equation:

$$\delta W_p + \delta W_v - \omega^2 \delta W_k = 0. \quad (\text{F.1})$$

The internal plasma potential energy is

$$\delta W_p = \frac{1}{2} \int \int \int d^3x [Q_2^2 + \Gamma p (\nabla \cdot \vec{\xi})^2 + \vec{J} \times \vec{\xi} \cdot \vec{Q}_2 + (\vec{\xi} \cdot \nabla p) (\nabla \cdot \vec{\xi})], \quad (\text{F.2})$$

where $\vec{Q}_2 = \nabla \times (\vec{\xi} \times \vec{B})$ is the perturbed magnetic field and Γ is the adiabatic index. The vacuum model presented in this paper is applicable to discretised vacuum domains, in particular, the mass-less, pressure-less and shear-less pseudo-plasma approach in TERPSICHORE. This pseudo-magnetic field and pseudo-displacement vector in the vacuum region are defined as \vec{T} and $\vec{\xi}_v$, respectively, and the perturbed magnetic field vector potential in the vacuum region, $\vec{A} = \vec{\xi}_v \times \vec{T}$, has no component parallel to \vec{T} (Schwenn *et al.* 1990). The magnetic energy in the vacuum region is

$$\delta W_v = \frac{1}{2} \int \int \int d^3x [\nabla \times (\vec{\xi}_v \times \vec{T})]^2. \quad (\text{F.3})$$

A useful description of the kinetic energy is the expression

$$\delta W_k = \frac{1}{2} \int \int \int d^3x \vec{\xi} \cdot \vec{\rho}_M \cdot \vec{\xi}, \quad (\text{F.4})$$

where $\vec{\rho}_M$ is the dyadic tensor given by

$$\vec{\rho}_M = \nabla s \nabla s + (\psi'_i(s) \nabla \theta - \psi'_p(s) \nabla \phi) (\psi'_i(s) \nabla \theta - \psi'_p(s) \nabla \phi). \quad (\text{F.5})$$

The eigenvalue of the system is ω^2 , with $\omega^2 < 0$ indicating instability. The applications of the TERPSICHORE code rely on a model kinetic energy that annihilates the parallel component of the perturbed displacement vector. This allows the algebraic elimination of the plasma compression term in the energy principle. Consequently, the incompressibility constraint is automatically applied and implies that $\nabla \cdot \vec{\xi} = 0$. The incompressibility constraint coupled with a model kinetic energy that annihilates the component of $\vec{\xi}$ parallel to \vec{B} , through the choice of the dyadic $\vec{\rho}_M$, reduces the linear ideal MHD stability problem to a partial differential equation with two unknowns, the component normal to the magnetic flux surfaces and a second binormal component. A Fourier decomposition of the perturbations in the Boozer magnetic coordinate system (Boozer 1981) and a radial discretisation with a hybrid finite element scheme further reduce the problem to a special block pentadiagonal matrix equation that is solved in the TERPSICHORE code with an inverse vector iteration method (Anderson *et al.* 1990). Vacuum pseudo-flux surfaces are constructed such that the geometry is continuously differentiable across the plasma vacuum interface into the vacuum domain. The structure of the matrix equation in the vacuum is identical to that in the plasma (Cooper 1992).

In a magnetically confined plasma, any perturbation must vanish at infinity. To approximate this condition, an axisymmetric conducting wall that hugs the major

axis, yet is sufficiently far from the plasma vacuum interface, is prescribed on which the radial component of the displacement vector $\xi_V \cdot \nabla s \equiv 0$.

TERPSICHORE has been applied for approximately 35 years for Stellarator and some Tokamak applications. It has been benchmarked with the CAS3D code (Nührenberg *et al.* 2009) and with 3-D finite-n ballooning corrections (Cooper, Singleton & Dewar 1996).

F.1 Resolution and mode families

For the TERPSICHORE analysis performed in this work, the radial resolution covered 123 radial intervals in the plasma and 36 in the vacuum domain. In the course of the work, the radial resolution of some MHD solutions was increased up to 165 (164 radial intervals) to investigate the radial convergence of localised perturbations. The $n=0$, $n=1$ and $n=2$ mode families were each explored. For a full description of the mode coupling that is implied by these families, please see Section 3 of Ardelea & Cooper (1997). The Fourier mode window was adjusted to encompass a spectrum of nearly 19 poloidal modes and between 10 and 17 toroidal modes (depending on whether the toroidal mode number is even or odd) about the dominant Fourier mode. This is adequate to couple the instability structure with the spectrum that describes the equilibrium state. This resolution was acceptable for low and intermediate m,n mode number structures because the configuration studied has low magnetic shear. In devices with higher shear, a finer radial grid would be required.

REFERENCES

- ALBERT, C.G., BEIDLER, C.D., KAPPER, G., KASILOV, S.V. & KERNBICHLER, W. 2024 On the convergence of bootstrap current to the Shaing-Callen limit in stellarators. arXiv: [2407.21599](https://arxiv.org/abs/2407.21599)
- ALEJNIKOVA, K. *et al.* 2021 Model for current drive induced crash cycles in W7-X. *Nucl. Fusion* **61** (12), 126040.
- ANDERSON, D.V., COOPER, W.A., GRUBER, R., MERAZZI, S. & SCHWENN, U. 1990 Methods for the efficient calculation of the mhd magnetohydrodynamic stability properties of magnetically confined fusion plasmas. *Intl J. High Performance Comput. Applics.* **4** (3), 34–47.
- ANDREEVA, T., BRÄUER, T., ENDLER, M., KISSLINGER, J. & IGITKHANOV, Y. 2004 Analysis of the magnetic field perturbations during the assembly of Wendelstein 7-X. *Fusion Sci. Technol.* **46** (2), 388–394.
- ANDREEVA, T. *et al.* 2022, Magnetic configuration scans during divertor operation of Wendelstein 7-X. *Nucl. Fusion* **62** (2), 026032.
- ARCHMILLER, M.C. *et al.* 2014 Suppression of vertical instability in elongated current-carrying plasmas by applying stellarator rotational transform. *Phys. Plasmas* **21** (5), 056113.
- ARDELEA, A. & COOPER, W.A. 1997 External kinks in plasmas with helical boundary deformation and net toroidal current. *Phys. Plasmas* **4** (10), 3482–3492.
- BADER, A. *et al.* 2025 Power and particle exhaust for the infinity two fusion pilot plant. *J. Plasma Phys.* **91**, E67.
- BAILLOD, A., LOIZU, J., QU, Z.S., ARBEZ, H.P. & GRAVES, J.P. 2023 Equilibrium beta-limits dependence on bootstrap current in classical stellarators. *J. Plasma Phys.* **89** (5), 905890508.
- BAUER, F., BETANCOURT, O. & GARABEDIAN, P.A. 1984 *Magnetohydrodynamic Equilibrium and Stability of Stellarators*. Springer.
- BEIDLER, C. *et al.* 1990 Physics and engineering design for Wendelstein VII-X. *Fusion Technol.* **17** (1), 148–168.
- BERNSTEIN, I.B., FRIEMAN, E.A., KRUSKAL, M.D. & KULSRUD, R.M. 1958 An energy principle for hydromagnetic stability problems. *Proc. R. Soc. Lond. Math. Phys. Sci.* **A244** (1236), 17–40.

- BICKERTON, R.J., CONNOR, J.W. & TAYLOR, J.B. 1971 Diffusion driven plasma currents and bootstrap tokamak. *Nat. Phys. Sci.* **229** (4), 110–112.
- BOOZER, A.H. 1981 Plasma equilibrium with rational magnetic flux surfaces. *Phys. Fluids* **24** (11), 1999–2003.
- BOOZER, A.H. & GARDNER, H.J. 1990 The bootstrap current in stellarators. *Phys. Fluids B: Plasma Phys.* **2** (10), 2408–2421.
- CARBAJAL, L. 2025 Alpha-particle confinement in Infinity Two Fusion Pilot Plant baseline plasma design. *J. Plasma Phys.* 1–30.
- CARRERAS, B.A., DOMINGUEZ, N., GARCIA, L., LYNCH, V.E., LYON, J.F., CARY, J.R., HANSON, J.D. & NAVARRO, A.P. 1988 Low-aspect-ratio torsatron configurations. *Nucl. Fusion* **28** (7), 1195–1207.
- CARY, J.R. & HANSON, J.D. 1986 Stochasticity reduction. *Phys. Fluids* **29** (8), 2464–2473.
- CATTANEL, G. *et al.* 1985 Influence of the magnetic configuration on plasma behaviour in the wendelstein vii-a stellarator. In *Controlled Fusion and Plasma Physics, Proc. 12th European Conf. Budapest, Part 1*, pp. 393. European Physical Society.
- COOPER, A. 1992 Variational formulation of the linear MHD stability of 3D plasmas with noninteracting hot electrons. *Plasma Phys. Control. Fusion* **34** (6), 1011–1036.
- COOPER, W.A., SINGLETON, D.B. & DEWAR, R.L. 1996 Spectrum of ballooning instabilities in a stellarator. *Phys. Plasmas* **3** (1), 275–280.
- CORREA-RESTREPO, D. 1978 Ballooning modes in three-dimensional MHD equilibria with shear. *Z. Naturforsch. A* **33** (7), 789–791.
- DEWAR, R.L. & HUDSON, S.R. 1998 Stellarator symmetry. *Physica D: Nonlinear Phenom.* **112** (1), 275–280.
- ERCKMANN, V. *et al.* 2007 Electron cyclotron heating for W7-X: physics and technology. *Fusion Sci. Technol.* **52** (2), 291–312.
- FABER, B. & BADER, A. 2024a MagneticFieldToolkit.jl. <https://gitlab.com/wistell/MagneticFieldToolkit.jl>
- FABER, B. & BADER, A. 2024b StellaratorOptimizationMetrics.jl. <https://gitlab.com/wistell/StellaratorOptimizationMetrics.jl>
- FENG, Y. *et al.* 2021 Understanding detachment of the W7-X island divertor. *Nucl. Fusion* **61** (8), 086012.
- FENG, Y., KOBAYASHI, M., LUNT, T. & REITER, D. 2011 Comparison between stellarator and tokamak divertor transport. *Plasma Phys. Control. Fusion* **53** (2), 024009.
- FREIDBERG, J.P. 2014 *Ideal MHD*. Cambridge University Press.
- FUJIWARA, M. *et al.* 2001 Overview of LHD experiments. *Nucl. Fusion* **41** (10), 1355–1367.
- GALEEV, A.A. & SAGDEEV, R.Z. 1968 Transport phenomena in a collisionless plasma in a toroidal magnetic system. *Sov. Phys. JETP* **26** (1), 233–240.
- GEIGER, J., NÜHRENBURG, C., GAO, YU, ANDREEVA, T., BRANDT, C., RAHBARNIA, K., THOMSEN, H. & the W7-X Team 2023 Low-shear configurations to test MHD-stability in Wendelstein 7-X. In *49th EPS Conference on Contr. Fusion and Plasma Phys*, European Physical Society, P4.064.
- GEIGER, J.E., WELLER, A., ZARNSTORFF, M.C., NÜHRENBURG, C., WERNER, A.H.F. & KOLESNICHENKO, Y.I. 2004 Equilibrium and stability of high-beta plasmas in Wendelstein 7-AS. *Fusion Sci. Technol.* **46** (1), 13–23.
- GORI, S., LOTZ, W. & NÜHRENBURG, J. 1997 Quasi-isodynamic stellarators. In *Theory of Fusion Plasmas (Proc. Joint Varenna-Lausanne Int. Workshop, (Bologna: Editrice Compositori))*, Società Italiana di Fisica, pp. 335–342.
- GRIEGER, G. *et al.* 1992 Physics optimization of stellarators. *Phys. Fluids B: Plasma Phys.* **4** (7), 2081–2091.
- GRIEGER, G., OHLENDORF, W., PACHER, H.D., WOBIG, H. & WOLF, G.H. 1971 Particle-confinement minima in the Wendelstein II-A-stellarator. In *Plasma Physics and Controlled Nuclear Fusion Research, Proc. of the 4th Int. Conf. Madison*, pp. 37–48. IAEA Vienna.
- GRIGULL, P. *et al.* 2001 First island divertor experiments on the W7-AS stellarator. *Plasma Phys. Control. Fusion* **43** (12A), A175–A193.
- GUTTENFELDER, W. *et al.* 2025 Predictions of core plasma performance for high field stellarator fusion pilot plants. *J. Plasma Phys.*

- HANSON, J.D. *et al.* 2013 Non-axisymmetric equilibrium reconstruction for stellarators, reversed field pinches and tokamaks. *Nucl. Fusion* **53** (8), 083016.
- HANSON, J.D. & CARY, J.R. 1984 Elimination of stochasticity in stellarators. *Phys. Fluids* **27** (4), 767–769.
- HANSON, J.D., HIRSHMAN, S.P., KNOWLTON, S.F., LAO, L.L., LAZARUS, E.A. & SHIELDS, J.M. 2009 V3FIT: a code for three-dimensional equilibrium reconstruction. *Nucl. Fusion* **49** (7), 075031.
- HARRIS, J.H. *et al.* 1984 Magnetohydrodynamic activity in high- β , currentless plasmas in heliotron-*e*. *Phys. Rev. Lett.* **53**, 2242–2245.
- HARTWELL, G.J. *et al.* 2013 Overview of results from the compact toroidal hybrid experiment. *40th EPS Conference on Plasma Physics*, Helsinki, Finland, European Physical Society. P2.102.
- HEGNA, C.C. 2011 Healing of magnetic islands in stellarators by plasma flow. *Nucl. Fusion* **51** (11), 113017.
- HEGNA, C.C. *et al.* 2025 The infinity two fusion pilot plant baseline plasma physics design. *J. Plasma Phys.* 1–44.
- HEGNA, C.C. & NAKAJIMA, N. 1998 On the stability of Mercier and ballooning modes in stellarator configurations. *Phys. Plasmas* **5** (5), 1336–1344.
- HELANDER, P. 2014 Theory of plasma confinement in non-axisymmetric magnetic fields. *Rep. Prog. Phys.* **77** (8), 087001.
- HELANDER, P. *et al.* 2012 Stellarator and tokamak plasmas: a comparison. *Plasma Phys. Control. Fusion* **54** (12), 124009.
- HELANDER, P. & NÜHRENBURG, J. 2009 Bootstrap current and neoclassical transport in quasi-isodynamic stellarators. *Plasma Phys. Control. Fusion* **51** (5), 055004.
- HELANDER, P., PARRA, F.I. & NEWTON, S.L. 2017 Stellarator bootstrap current and plasma flow velocity at low collisionality. *J. Plasma Phys.* **83** (2), 905830206.
- HELANDER, P. & SIGMAR, D.J. 2005 *Collisional Transport in Magnetized Plasmas*. Vol. 4. Cambridge University Press.
- HINTON, F.L. & HAZELTINE, R.D. 1976 Theory of plasma transport in toroidal confinement systems. *Rev. Mod. Phys.* **48** (2), 239–308.
- HIRSCH, M. *et al.* 2008 Major results from the stellarator Wendelstein 7-AS. *Plasma Phys. Control. Fusion* **50** (5), 053001.
- HIRSHMAN, S.P. *et al.* 1986 Three-dimensional free boundary calculations using a spectral Green's function method. *Comput. Phys. Commun.* **43** (1), 143–155.
- HIRSHMAN, S.P. & WHITSON, J.C. 1983 Steepest-descent moment method for three-dimensional magnetohydrodynamic equilibria. *Phys. Fluids* **26** (12), 3553–3568.
- HUDSON, S.R., DEWAR, R.L., DENNIS, G., HOLE, M.J., MCGANN, M., VON NESSI, G. & LAZERSON, S. 2012 Computation of multi-region relaxed magnetohydrodynamic equilibria. *Phys. Plasmas* **19** (11), 112502.
- JAKUBOWSKI, M. *et al.* 2021 Overview of the results from divertor experiments with attached and detached plasmas at Wendelstein 7-X and their implications for steady-state operation. *Nucl. Fusion* **61** (10), 106003.
- KISSLINGER, J. & ANDREEVA, T. 2005 Correction possibilities of magnetic field errors in Wendelstein 7-X. *Fusion Engng Des.* **74** (1), 623–626.
- KOMORI, A. *et al.* 2006 Overview of progress in LHD experiments. *Fusion Sci. Technol.* **50** (2), 136–145.
- KRUSKAL, M.D. & KULSRUD, R.M. 1958 Equilibrium of a magnetically confined plasma in a toroid. *Phys. Fluids* **1** (4), 265–274.
- KUMAR, A. *et al.* 2022 Nature of ideal MHD instabilities as described by multi-region relaxed MHD. *Plasma Phys. Control. Fusion* **64** (6), 065001.
- LANDREMAN, M. 2017 An improved current potential method for fast computation of stellarator coil shapes. *Nucl. Fusion* **57** (4), 046003.
- LANDREMAN, M., BULLER, S. & DREVLAK, M. 2022 Optimization of quasi-symmetric stellarators with self-consistent bootstrap current and energetic particle confinement. *Phys. Plasmas* **29** (8), 082501.
- LANDREMAN, M. & CATTO, P.J. 2012 Omnigenity as generalized quasisymmetry. *Phys. Plasmas* **19** (5), 056103.

- LANDREMAN, M., SMITH, H.M., MOLLÉN, A. & HELANDER, P. 2014 Comparison of particle trajectories and collision operators for collisional transport in nonaxisymmetric plasmas. *Phys. Plasmas* **21** (4), 042503.
- MAASSBERG, H., BURHENN, R., GASPARINO, U., KÜHNER, G., RINGLER, H. & DYABILIN, K.S. 1993 Experimental and neoclassical electron heat transport in the LMFP regime for the stellarators W7-A, L-2, and W7-AS. *Phys. Fluids B: Plasma Phys.* **5** (10), 3627–3640.
- MEISS, J.D. 1992 Symplectic maps, variational principles, and transport. *Rev. Mod. Phys.* **64** (3), 795–848.
- MERCIER, C. 1962 Critère de stabilité d'un système toroïdal hydromagnétique en pression scalaire. In *Plasma Physics and Controlled Nuclear Fusion Research 1961*, *Nucl. Fusion Suppl.*, vol. 2, pp. 801, International Atomic Energy Agency.
- MERKEL, P. 1987 Solution of stellarator boundary value problems with external currents. *Nucl. Fusion* **27** (5), 867–871.
- MIYAMOTO, K. 1987 *Plasma Physics for Nuclear Fusion*. The MIT Press.
- MORISAKI, T. *et al.* 2005 Local island divertor experiments on LHD. *J. Nucl. Mater.* **337-339**, 154–160. pSI-16
- MOTOJIMA, O. *et al.* 1985 Studies of currentless, high-beta plasma in the Heliotron E device. *Nucl. Fusion* **25** (12), 1783–1787.
- NAKAJIMA, N., OKAMOTO, M., TODOROKI, J., NAKAMURA, Y. & WAKATANI, M. 1989 Optimization of the bootstrap current in a large helical system with $L = 2$. *Nucl. Fusion* **29** (4), 605–616.
- NARUSHIMA, Y., WATANABE, K.Y., SAKAKIBARA, S., NARIHARA, K., YAMADA, I., SUZUKI, Y., OHDACHI, S., OHYABU, N., YAMADA, H. & NAKAMURA, Y. 2008 Dependence of spontaneous growth and suppression of the magnetic island on beta and collisionality in the LHD. *Nucl. Fusion* **48** (7), 075010.
- NÜHRENBURG, C., BOOZER, A.H. & HUDSON, S.R. 2009 Magnetic-surface quality in nonaxisymmetric plasma equilibria. *Phys. Rev. Lett.* **102** (23), 235001.
- PANDYA, M.D. *et al.* 2015 Low edge safety factor operation and passive disruption avoidance in current carrying plasmas by the addition of stellarator rotational transform. *Phys. Plasmas* **22** (11), 110702.
- PFIRSCH, D. & SCHLÜTER, A. 1962 Max Planck Institute, Munich, Report MPI/PA/7/62.
- RAMASAMY, R., ALEYNIKOVA, K., NIKULSIN, N., HINDENLANG, F., HOLOD, I., STRUMBERGER, E., HOELZL, M. & the JOREK team Nonlinear MHD modeling of soft limits in W7-AS. *Nucl. Fusion* **64** (8), 086030.
- REIMAN, A. *et al.* 2007 Equilibrium and flux surface issues in the design of the NCSX. *Fusion Sci. Technol.* **51** (2), 145–165.
- RENNER, H., BOSCARY, J., ERCKMANN, V., GREUNER, H., GROTE, H., SAPPER, J., SPETH, E., WESNER, F. & WANNER, M. 2000 The capabilities of steady state operation at the stellarator W7-X with emphasis on divertor design. *Nucl. Fusion* **40** (6), 1083–1093.
- RISSE, K., RUMMEL, T., BOSCH, H.-S., BYKOV, V., CARLS, A., FÜLLENBACH, F., MÖNNICH, T., NAGEL, M. & SCHNEIDER, M. 2018 The magnet system of Wendelstein 7-X stellarator in operation. *Fusion Engng Des.* **136**, 12–16.
- SAKAKIBARA, S. *et al.* 2001 MHD characteristics in the high beta regime of the Large Helical Device. *Nucl. Fusion* **41** (9), 1177–1183.
- SANCHEZ, R., HIRSHMAN, S.P. & WARE, A.S. 2000 COBRA: an optimized code for fast evaluation of ideal ballooning stability of three dimensional equilibria. *J. Comput. Phys.* **161** (2), 576–588.
- SANCHEZ, R. *et al.* 2001 Ideal MHD stability calculations for compact stellarators. *Comput. Phys. Commun.* **141** (1), 55–65.
- SCHLUTT, M.G., HEGNA, C.C., SOVINEC, C.R., HELD, E.D. & KRUGER, S.E. 2013 Self-consistent simulations of nonlinear magnetohydrodynamics and profile evolution in stellarator configurations. *Phys. Plasmas* **20** (5), 056104.
- SCHWENN, U., ANDERSON, D.V., COOPER, W.A., GRUBER, R. & MERAZZI, S. 1990 Global ideal MHD stability of 3D plasmas with pseudo-vacuum treatment for free-boundary modes. *Scientific Computing on Supercomputers II*, Plenum Press, 159–174.
- SHAFRANOV, V.D. 1963 Equilibrium of a toroidal pinch in a magnetic field. *Sov. Atomic Energy* **13** (6), 1149–1158.

- SHAING, K.-C. 1984 Stability of the radial electric field in a nonaxisymmetric torus. *Phys. Fluids* **27** (7), 1567–1569.
- SHAING, K.-C. & CALLEN, J.D. 1983 Neoclassical flows and transport in nonaxisymmetric toroidal plasmas. *Phys. Fluids* **26** (11), 3315–3326.
- SMIET, C.B., LOIZU, J., BALKOVIC, E. & BAILLOD, A. 2025 Efficient single-stage optimization of islands in finite-beta stellarator equilibria. *Phys. Plasmas* **32** (1), 012504.
- SOVINEC, C., CORNILLE, B., GUPTA, U., INGRAM, A., MCCOLLAM, K., PATIL, S., SAINTERME, A. & TILLINGHAST, G. 2022 Overview of NIMROD modeling at the University of Wisconsin-Madison. In *APS Division of Plasma Physics Meeting Abstracts, APS Meeting Abstracts*, vol. 2022, pp. BP11.021. AIP Publishing.
- SPONG, D.A., HIRSHMAN, S.P., LYON, J.F., BERRY, L.A. & STRICKLER, D.J. 2005 Recent advances in quasi-poloidal stellarator physics issues. *Nucl. Fusion* **45** (8), 918–925.
- SUZUKI, Y. 2017 HINT modeling of three-dimensional tokamaks with resonant magnetic perturbation. *Plasma Phys. Control. Fusion* **59** (5), 054008.
- SUZUKI, Y., NAKAJIMA, N., WATANABE, K., NAKAMURA, Y. & HAYASHI, T. 2006 Takaya 2006 Development and application of HINT2 to helical system plasmas. *Nucl. Fusion* **46** (11), L19.
- W VII-A Team 1980 Stabilization of the (2, 1) tearing mode and of the current disruption in the W VII-A stellarator. *Nucl. Fusion* **20** (9), 1093–1100.
- TURKIN, YU, BEIDLER, C.D., MAASSBERG, H., MURAKAMI, S., TRIBALDOS, V. & WAKASA, A. 2011 Neoclassical transport simulations for stellarators. *Phys. Plasmas* **18** (2), 022505.
- VARELA, J., WATANABE, K.Y., NAKAJIMA, N., OHDACHI, S., GARCIA, L. & MIER, J.A. 2011 Ballooning modes instabilities in outward LHD configurations. *Plasma Fusion Res.* **6**, 1403013.
- WAKATANI, M. 1998 *Stellarator and Heliotron Devices*. Oxford University Press.
- WATANABE, K., NAKAJIMA, N., OKAMOTO, M., NAKAMURA, Y. & WAKATANI, M. 1992 Three-dimensional MHD equilibrium in the presence of bootstrap current for the Large Helical Device. *Nucl. Fusion* **32** (9), 1499–1513.
- WELLER, A. *et al.* 2003 Experiments close to the beta-limit in W7-AS. *Plasma Phys. Control. Fusion* **45** (12A), A285.
- WRIGHT, A.M. & FERRARO, N.M. 2024 MHD-induced beta limits in the Large Helical Device. *Phys. Plasmas* **31** (10), 102509.
- YAMADA, H. 2011 Overview of results from the Large Helical Device. *Nucl. Fusion* **51** (9), 094021.
- ZANINI, M. *et al.* 2021 Confinement degradation and plasma loss induced by strong sawtooth crashes at W7-X. *Nucl. Fusion* **61** (11), 116053.
- ZANINI, M. *et al.* 2020 ECCD-induced sawtooth crashes at W7-X. *Nucl. Fusion* **60** (10), 106021.
- ZHOU, Y., ALEYNIKOVA, K., LIU, C. & FERRARO, N.M. 2024 Benign saturation of ideal ballooning instability in a high-performance stellarator. *Phys. Rev. Lett.* **133** (13), 135102.
- ZHU, C., HUDSON, S.R., SONG, Y. & WAN, Y. 2018 Designing stellarator coils by a modified newton method using focus. *Plasma Phys. Control. Fusion* **60** (6), 065008.